Glacial/interglacial wetland, biomass burning, and geologic methane emissions constrained by dual stable isotopic CH_4 ice core records

Michael Bock[a,b,1], Jochen Schmitt[a,b], Jonas Beck[a,b], Barbara Seth[a,b], Jérôme Chappellaz[c,d,e,f], and Hubertus Fischer[a,b,1]

[a]Climate and Environmental Physics, Physics Institute, University of Bern, 3012 Bern, Switzerland; [b]Oeschger Centre for Climate Change Research, University of Bern, 3012 Bern, Switzerland; [c]CNRS, IGE (Institut des Géosciences de l'Environnement), F-38000 Grenoble, France; [d]University of Grenoble Alpes, IGE, F-38000 Grenoble, France; [e]IRD (Institut de Recherche pour le Développement), IGE, F-38000 Grenoble, France; and [f]Grenoble INP (Institut National Polytechnique), IGE, F-38000 Grenoble, France

Edited by Mark H. Thiemens, University of California at San Diego, La Jolla, CA, and approved June 1, 2017 (received for review August 20, 2016)

Atmospheric methane (CH_4) records reconstructed from polar ice cores represent an integrated view on processes predominantly taking place in the terrestrial biogeosphere. Here, we present dual stable isotopic methane records [$\delta^{13}CH_4$ and $\delta D(CH_4)$] from four Antarctic ice cores, which provide improved constraints on past changes in natural methane sources. Our isotope data show that tropical wetlands and seasonally inundated floodplains are most likely the controlling sources of atmospheric methane variations for the current and two older interglacials and their preceding glacial maxima. The changes in these sources are steered by variations in temperature, precipitation, and the water table as modulated by insolation, (local) sea level, and monsoon intensity. Based on our $\delta D(CH_4)$ constraint, it seems that geologic emissions of methane may play a steady but only minor role in atmospheric CH_4 changes and that the glacial budget is not dominated by these sources. Superimposed on the glacial/interglacial variations is a marked difference in both isotope records, with systematically higher values during the last 25,000 y compared with older time periods. This shift cannot be explained by climatic changes. Rather, our isotopic methane budget points to a marked increase in fire activity, possibly caused by biome changes and accumulation of fuel related to the late Pleistocene megafauna extinction, which took place in the course of the last glacial.

atmosphere | methane | megafauna | ice core | stable isotopes

Past variations of the atmospheric methane mixing ratio ($[CH_4]$) have been documented using ice cores on various timescales (1–5). Compared with preindustrial levels of 715 parts per billion (ppb) (6, 7), anthropogenic emissions have led to a 2.5-fold increase since about the year 1800 CE as documented by the National Oceanic and Atmospheric Administration Earth System Research Laboratory. The lowest values of around 360 ppb are measured in ice cores during glacial maxima, whereas for the last eight interglacials, $[CH_4]$ typically ranged between 600 and 700 ppb (4). Fast and significant stadial/interstadial $[CH_4]$ increases occurred within a few decades during glacials in parallel to Dansgaard–Oeschger events (8). Furthermore, $[CH_4]$ levels in the Northern Hemisphere are mostly higher than those in the Southern Hemisphere (9). These data taken together with our understanding of the present day methane budget (10–15) show that wetlands and primarily those located in the tropics dominate natural CH_4 emissions. On long timescales, wetland extent (16) and CH_4 fluxes are also strongly influenced by the position of the Intertropical Convergence Zone (ITCZ) (17) and the global monsoon system (18, 19), which in turn, is steered by changes in solar insolation. There is an ongoing debate on the relative contributions from tropical vs. boreal wetlands (ref. 9 and references therein). The latter is possibly overestimated, because other high-latitude sources, like thawing permafrost, thermokarst lakes (20), or (cryospherically capped) geologic seeps (21), also contribute to this source from a hemispheric (ice core) point of view.

Additional constraints on the contribution of the various methane sources can be derived from the carbon and hydrogen stable isotopic signature of CH_4 in ice cores. Microbially produced CH_4 is depleted in both stable isotopologues (^{13}C and ^{2}H or D; "light" isotopic sources) compared with the source mix. However, there are two important natural sources relatively enriched in ^{13}C and D ("heavy" sources): biomass burning (BB), an important and climatically variable process (22–26), and "geologic" emissions of old methane (GEMs; called GEM by, for example, refs. 27–29).

Accordingly, the isotopic fingerprint of methane has been successfully used to shed light on relative source mix changes (30–33). However, biogenic sources (such as wetlands and BB) may change their isotopic signatures in parallel to changing climate and environmental conditions (25, 34). For the last glacial, Möller et al. (25) showed that the ^{13}C content of CH_4 ($\delta^{13}CH_4$) is higher at low CO_2 levels and concluded that biome changes play a major role in this isotopic change. The deuterium content of CH_4 [$\delta D(CH_4)$] is also a function of the isotopic signature of the water used for methanogenesis (31, 35–38). However, the net impact of global meteoric water isotope changes caused by the transfer of water from the ocean to ice sheets is only of secondary importance (refs. 31 and 36 and references therein). Both $\delta^{13}CH_4$ and $\delta D(CH_4)$ are influenced by at least one other factor, namely the ratio of net to gross CH_4 production in wetlands (i.e., the fraction of CH_4 consumed by methanotrophs before emission to the atmosphere). This process varies as a function of the water table and site conditions, leading to changes in strength and isotopic composition of CH_4 emissions (31, 39).

Significance

Polar ice is a unique archive of past atmosphere. Here, we present methane stable isotope records (used as source fingerprint) for the current and two past interglacials and their preceding glacial maxima. Our data are used to constrain global emissions of methane. Tropical wetlands and floodplains seem to be the dominant sources of atmospheric methane changes, steered by past variations in sea level, monsoon intensity, temperature, and the water table. In contrast, geologic emissions of methane are stable over a wide range of climatic conditions. The long-term shift seen in both isotopes for the last 25,000 y compared with older intervals is likely connected to changes in the terrestrial biosphere and fire regimes as a consequence of megafauna extinction.

Author contributions: M.B., J.S., and H.F. designed research; M.B., J.S., and B.S. performed research; M.B. and J.S. contributed new reagents/analytic tools; M.B., J.S., J.B., and H.F. analyzed data; M.B. performed methane box modeling; J.B. performed methane box modeling and firn diffusion correction; M.B., J.S., J.B., and H.F. prepared the discussion of results; and M.B., J.S., J.C., and H.F. wrote the paper.

The authors declare no conflict of interest.

This article is a PNAS Direct Submission.

Data deposition: The ice core data reported in this paper are available at https://doi.pangaea.de/10.1594/PANGAEA.873918.

[1]To whom correspondence may be addressed. Email: bock@climate.unibe.ch or hubertus.fischer@climate.unibe.ch.

This article contains supporting information online at www.pnas.org/lookup/suppl/doi:10.1073/pnas.1613883114/-/DCSupplemental.

In this contribution, we greatly extend the existing carbon and hydrogen isotopic information of CH_4 from ice cores in terms of temporal coverage, temporal resolution, accuracy, and precision. Our data cover three interglacials and their preceding glacial terminations and glacial maxima. The interpretation of these data centers around the discussion of the source side of the methane cycle. This assumption is justified in the light of recent work on sinks of methane (40–43), with net variations that are estimated to be relatively small (*SI Text*). Hence, dual stable isotope records of methane provide important insights into the suite of terrestrial and marine processes emitting methane and their changes in the past.

Ice Core Measurements

We measured records of methane stable carbon ($\delta^{13}CH_4$) and hydrogen [$\delta D(CH_4)$] isotopes from four Antarctic ice cores (Fig. 1 and Figs. S1 and S2–S5): i.e., the two European Project for Ice Coring in Antarctica (EPICA) ice cores from Dronning Maud Land (EDML) and from Dome Concordia (EDC), the Talos Dome [Talos Dome Ice Core Project (TALDICE)], and the Vostok (core 5G; Vostok Station) ice cores. Note that these values are representative of the tropospheric isotope signature of methane in high southern latitudes and that an interpolar difference (IPD) in [CH_4] and its isotopic signatures exists.

The investigated time periods are from 25 to 0.5 kilo years (ka) before present [(BP), where present refers to 1950], from 160 to 80 ka BP, and from 440 to 370 ka BP (Fig. 1 and Fig. S1). With reference to marine sediment records, these time periods are approximately equivalent to Marine Isotope Stage (MIS) 2&1, MIS 6&5.5, and MIS 12&11.3, respectively (44, 45).

The $\delta^{13}CH_4$ data were measured on the TALDICE (170 samples) and EDC (90 samples) ice cores and using seven samples from Vostok for MIS 5.5. For $\delta D(CH_4)$, we present data from EDML (54 samples) for MIS 2&1 and MIS 5.5 and from EDC (47 samples) for MIS 6&5.5 and MIS 12&11.3. Altogether, this dataset presents dual stable isotope records from three glacial maxima, the following terminations and interglacials, and two glacial inceptions.

Information on measurement procedures, accuracy, and precision can be found in *Materials and Methods* and our technical papers (46–48). $\delta^{13}CH_4$ and $\delta D(CH_4)$ data are reported using the δ notation on the international Vienna Pee Dee Belemnite (VPDB) and Vienna Standard Mean Ocean Water (VSMOW) scales, respectively. Information on data handling with respect to firn diffusion effects is described in *SI Text*.

Results

The main results of this study, presented in Fig. 1 and Fig. S1, confirm previous results but largely extend the time coverage and are based on data with improved precision and accuracy (46–48). Our results are consistent with $\delta^{13}CH_4$ data from Greenland Ice Sheet Project 2 (GISP2) (49) and EDML (32) for the Holocene (MIS 1), the last termination, and the last glacial maximum (LGM) (Fig. 1 and Figs. S3 and S6), as well as throughout the last glacial period (25) (Fig. S1). For the last 25 ka, we present a greatly improved view of the evolution of $\delta D(CH_4)$ compared with the pioneering work by Sowers (31, 49), which was characterized by higher sample to sample variability (Fig. S6).

In our data, we document a rather smooth deglacial $\delta D(CH_4)$ decrease of 18‰ and only small long-term variations over the Holocene, with a mean value of −71‰ for the Southern Hemisphere. Note that there is a north–south IPD for $\delta D(CH_4)$ of roughly −16‰ for the Holocene (46). Interestingly, glacial/interglacial amplitudes in $\delta D(CH_4)$ can be either of similar amplitude (LGM–Holocene: ∼14‰) as swings from stadial to interstadial conditions (e.g., during the glacial inception around 390 ka BP in Fig. 1) or considerably larger (MIS 6–MIS 5: ∼25‰). The decrease of $\delta D(CH_4)$ into MIS 5.5 is also faster compared with the much smoother MIS 2/1 and MIS 12/11.3 transitions. On the contrary, all of the $\delta^{13}CH_4$ transitions investigated are gradual (Figs. S3–S5).

Within full glacial periods and interglacials, $\delta D(CH_4)$ shows rather small variations [standard deviation (SD) is typically around 5‰ (Table S1)] compared with the large leverage of sources and sinks, indicating little changes in the source composition. On the contrary, $\delta^{13}CH_4$ shows pronounced trends that differ for all of the interglacials investigated. Most importantly, interglacial $\delta^{13}CH_4$ is not correlated to [CH_4]. Next, while for $\delta D(CH_4)$ and $\delta^{13}CH_4$, the interglacial MIS 5.5 and MIS 11.3 mean levels are comparable, a clear shift of the mean values for the Holocene is evident (Fig. 1 and Fig. S2). A shift of similar size is also found for the mean level during the LGM compared with MIS 6 and MIS 12 (Fig. 1 and Table S1).

Our data confirm earlier findings (25, 49) that $\delta^{13}CH_4$ is evolving independently from [CH_4] for large parts of the ice core record. This feature is substantiated by new $\delta^{13}CH_4$ data from EDC over the MIS 12/11.3 transition and the penultimate glacial termination as well as for variations during MIS 11.3. In all of the terminations investigated, $\delta^{13}CH_4$ drops strongly when [CH_4] increases only slowly, well before the major rapid [CH_4] rise (Fig. 1 and Figs. S3–S5). Only about one-half of the amplitude of the $\delta^{13}CH_4$ change is covariant with the rapid methane rises into the interglacial periods. The decoupling between $\delta^{13}CH_4$ and [CH_4] is even more evident during rapid CH_4 rises connected to Dansgaard–Oeschger (DO) events, which have no counterpart in $\delta^{13}CH_4$. This observation is indicative of small source mix changes (25). Moreover, there is no abrupt $\delta^{13}CH_4$ shift connected to the [CH_4] peak during the early MIS 5.5 (128.5 ka BP) (Fig. 1). On the contrary, $\delta^{13}CH_4$ continues its downward trend during MIS 5.5, when [CH_4] decreases toward lower glacial values, whereas [CO_2] and $\delta^{15}N_2$ in ice cores (a proxy for firn temperature) indicate interglacial conditions (50, 51). $\delta^{13}CH_4$ only reverses its trend around 115 ka BP when [CO_2] and $\delta^{15}N_2$ start to drop (Fig. S4). At that point in time, [CH_4] is already below 500 ppb, a level typical of stadial intervals.

To confirm the very low $\delta^{13}CH_4$ values of our EDC and TALDICE records at the end of MIS 5.5 (which were not seen in the very few Vostok samples previously measured at Pennsylvania State University and presented in ref. 25), we analyzed an additional seven samples from the Vostok core with our improved method. These samples correspond well to our data from other ice cores (Fig. 1 and Fig. S4), thus indicating that the lowest values for $\delta^{13}CH_4$ of −52‰ must have been missed in the older Vostok record (25), most likely because of methodological problems. Other small differences in our record compared with the older Vostok time series are presented in figure 9 of ref. 47, but the overall conclusions of ref. 25 are confirmed in the light of the improved dataset presented here (Fig. 1 and Fig. S1).

Discussion

The Potential of Marine Clathrates and Other Geologic CH_4 Emissions.

Decreasing $\delta D(CH_4)$ over all three glacial terminations (Fig. 1) supports the conclusion in refs. 31 and 36 that marine clathrates (gas hydrates) do not significantly contribute to the altered atmospheric CH_4 budget during transitions. However, it is not only catastrophic emissions caused by destabilization events of marine clathrates that have been proposed to explain past [CH_4] variations (52, 53) but also, more steady emissions through, for example, natural marine hydrocarbon seeps that may have been exposed during times of sea-level low stands. Together with seeps and mud volcanoes, clathrate releases constitute the so-called GEM (27, 28, 54). Concerning the modern Arctic, there is also an ongoing debate on the origin and importance of CH_4 releases from the East Siberian Shelf (55–59), which are thought to stem from both organic carbon in thawing subsea permafrost and geologic reservoirs.

In the following section, we show that our isotope data (Fig. 1) are incompatible with the strong role of GEM proposed by, for

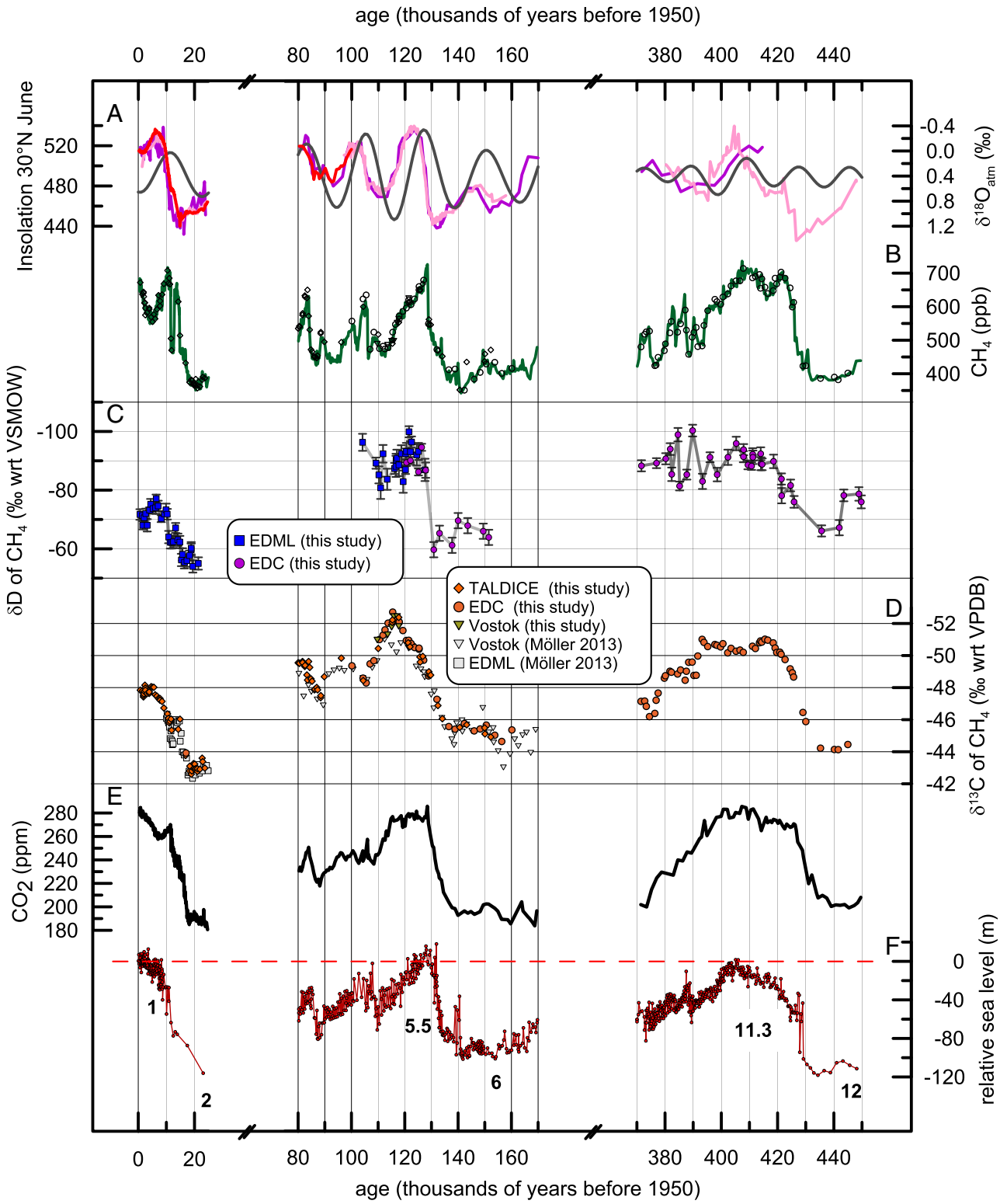

Fig. 1. Paleoclimatic records for three interglacials and preceding glacial maxima (note the breaks in the *x* axis). From top to bottom, the panels show (*A*) solar insolation in June at 30° N (133) and atmospheric $\delta^{18}O$ from Vostok (purple) (134), EDC (light pink) (51, 135–138), and Siple Dome (red) (84); (*B*) [CH_4] (ref. 4 and data from this study); (*C*) $\delta D(CH_4)$ from EDML and EDC (this study; error bars are 1-sigma SDs of reference air measurements); (*D*) $\delta^{13}CH_4$ from Talos Dome, EDC, and Vostok (5G; this study; the error [based on 1-sigma SDs of replicate ice core measurements (47)] is approximately the size of the symbols) and data from EDML and Vostok (25, 32); (*E*) [CO_2] (110); and (*F*) relative sea level as reconstructed from Red Sea sediment cores (108). Time intervals indicative of MIS (45) are given next to the sea-level curve. Ice core records are given on the Antarctic ice core chronology (AICC2012) gas age scale (137, 139), and insolation and sea level on their individual age scales. Note the inverse direction of all isotope axes.

example, refs. 29, 60, and 61. Luyendyk et al. (61) argue that lowered methane concentrations along with high $\delta^{13}CH_4$ values during the glacial could be a result of increased GEM, whereas wetland emissions were reduced to a minimum. However, our $\delta D(CH_4)$ constraint indicates that this hypothesis is incorrect for two reasons. First, the differences in $\delta D(CH_4)$ between glacials and interglacials are too small to be compatible with a dominant GEM source, and second, a covariation (e.g., within MIS 5.5) of $\delta^{13}CH_4$ and $\delta D(CH_4)$, expected under the dominant GEM hypothesis, is not seen in our data (Fig. 1 and Figs. S2–S5). An unambiguous assessment of the geologic emissions based on $^{14}CH_4$ measurements performed on Antarctic ice over the last termination is pending, but results presented by Petrenko et al. (62) indicate only a 10% contribution from GEM to the atmospheric methane budget during the Younger Dryas period and no strengthening of this source for the $[CH_4]$ rise into the Preboreal.

To quantify the maximum contribution of GEM based on our data, we used our previously described box model (32, 36). However, to be consistent with work on the recent atmospheric methane budget (63), we differentiated only three source categories (microbial, GEM, and BB). Emissions and isotopic signatures of these three sources were varied in our model within predefined limits in a Monte Carlo approach. Moreover, we also included a Cl sink for CH_4 in the marine boundary layer. Equilibrium results of each model run were compared with the ice core constraints (Table S1), and 10,000 valid runs were recorded for each time slice (details are in *Materials and Methods*, *SI Text*, and Fig. S7). Hence, all box model runs accepted in this study are consistent with the presented ice core constraints within the error limits of the data.

Here, we focus on the model results for GEM and BB presented in Fig. 2, showing a clear and expected anticorrelation of the emission strengths of the two sources (because both are enriched in ^{13}C and D relative to the microbial source). Moreover, Fig. 2 shows that, for any given GEM value, BB emissions are higher in the Holocene and the LGM compared with previous interglacials and glacials, respectively (*Biome and Fire Regime Changes Caused by Megafauna Extinction*). We can use Fig. 2 to constrain possible GEM, where we can safely assume that GEMs are the same during the Holocene compared with previous interglacials and the same for the LGM compared with previous glacial maxima. Our model results allow individual scenarios with higher GEMs for glacials compared with interglacials (Fig. 2). However, because BB emissions must always be larger than zero, an absolute upper limit of interglacial (glacial) GEM is 90 (70) Tg CH_4 a^{-1} (Terragram methane per year) according to our data constraints. Using independent estimates of Holocene and LGM BB emissions (10, 32, 36, 63–66) of 25 and 15 Tg CH_4 a^{-1}, respectively, GEMs are in fact smaller than 47 (Holocene) and 41 (LGM) Tg CH_4 a^{-1}. It is important to stress that our mean Holocene estimate is based on krypton-free $\delta^{13}CH_4$ data, resulting in lower $\delta^{13}CH_4$ values and thus, slightly lower GEMs compared with previous assessments (63, 64) of the Late Holocene (discussion is in *SI Text*).

Overall, we conclude that GEMs (seeps and marine clathrates) are at no point the dominant contributor to the global methane budget, and they are not strongly variable players that could explain the observed glacial/interglacial $[CH_4]$ variations over the last few hundreds of thousands of years (Figs. 1 and 2 and *SI Text*) (25, 31–33, 36, 62). Thus, we infer that microbial sources must represent the dominant control for natural atmospheric CH_4 changes.

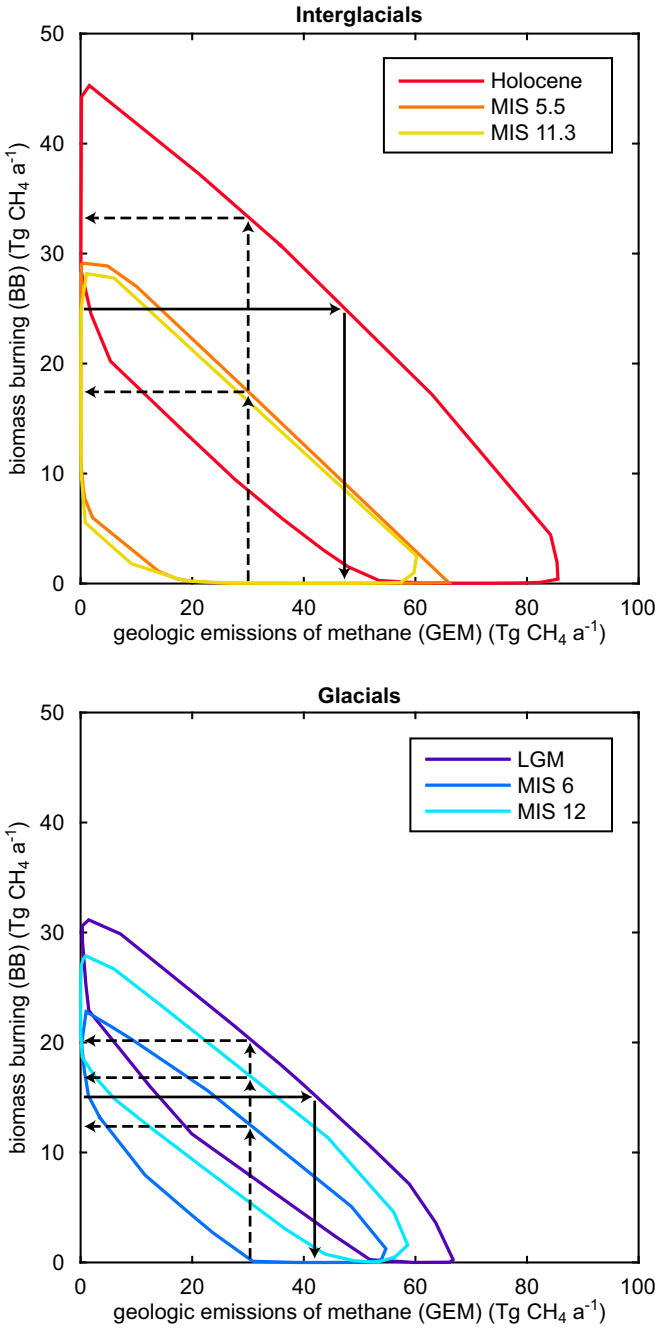

Fig. 2. Box model results fulfilling the ice core constraint. Shown are emission strengths of BB and GEM. Each envelope encloses all 10,000 valid realizations of the Monte Carlo processes searching the parameter spaces of the six time periods (*SI Text* and Table S1). The Matlab function convhull() was used to determine the envelope around the solutions for each time slice. *Upper* shows results for interglacials, and *Lower* shows results for glacials. Model results for the Holocene and the LGM are considerably shifted toward higher GEM and/or BB because of the ^{13}C- and D-enriched isotope targets of these younger time slices (Fig. 1 and Table S1). Arrows indicate possible readouts to assess maximal GEM for all investigated time periods (solid lines) and increased BB for the Holocene and the LGM compared with previous time periods (dashed lines).

The Role of High Northern Latitude Microbial Emissions. Recently, Köhler et al. (67) calculated that—dependent on assumptions on the gas age distribution of the bubbles in the ice—up to 14 Tg CH_4 a^{-1} could have been released into the atmosphere from permafrost thawing (a source relatively depleted in ^{13}C and D) over the Oldest Dryas–Bölling/Alleröd (OD-BA) transition. Unfortunately, the resolution of our $\delta D(CH_4)$ data for this event is insufficient to give a direct and qualified answer. For the

Younger Dryas–Preboreal (YD-PB) transition, Melton et al. (68) argued that it is possible to close the isotopic budget by a parallel increase in ^{13}C- and D-enriched emissions from BB and depleted emissions from thermokarst lakes. However, given our information on a gradual and modest decrease of $\delta D(CH_4)$ over this transition decoupled from the strong $[CH_4]$ increase (Fig. S3), this argumentation is only one valid scenario. We argue that a dominant contribution of D-depleted high-latitude emissions (in which we include thawing permafrost/thermokarst lakes/boreal wetland emissions) to the rapid CH_4 increases is unlikely, because the gradual decrease in $\delta D(CH_4)$ during the Preboreal starts only after $[CH_4]$ is already high (Fig. S3). For the Younger Dryas, $\delta D(CH_4)$ stays at −62‰ and does not change over the YD-PB transition. Also, there is no imprint of rapidly increasing ^{13}C-depleted emissions from northern high-latitude wetlands (as proposed in ref. 69) in the rather smooth evolution of $\delta^{13}CH_4$. For both rapid $[CH_4]$ rises (OD-BA and YD-PB), explanations are preferred that invoke increasing emissions of sources with small isotopic leverage on $\delta D(CH_4)$ and $\delta^{13}CH_4$ as the main drivers. This kind of emission change is fulfilled by strengthening low-latitude microbial sources, such as predominately C4-fed tropical wetlands, which incorporate increasingly depleted water (as seen in $\delta^{18}O$ records) during methanogenesis at that time (12, 35, 70).

For the Holocene, several authors have suggested higher CH_4 emissions from high-latitude ecosystems relative to the LGM (71–73). Based on pollen analyses, Yu et al. (73) proposed a protopeatland phase as the precursor for the succession from wetlands to fens and later bogs. Because peatlands evolve from fens to bogs, this succession is accompanied by decreasing CH_4 emissions and a shift to lower $\delta^{13}CH_4$ signatures. The latter may be linked to trophic status, degree of methanotrophy, plant types, or type and quality of organic substrates (49, 74–76). However, because there is a strong reduction of methane emissions during this succession, the source signature effect does not leave a sizable imprint in the CH_4 isotopic signature of the atmosphere. Accordingly, the observed leveling out of $\delta^{13}CH_4$ changes during the Holocene is in line with decreasing emissions from northern peatlands (49). To close the budget, the increase in $[CH_4]$ over the latest 4.5 ka calls for an additional source. Several theories have been put forward (42, 72, 77, 78), on which we comment below.

Control of (Sub-)Tropical Wetland and Floodplain Emissions on Atmospheric CH_4. Multiple lines of evidence suggest that (sub-) tropical (sporadically/seasonally inundated) floodplains, wetlands, and peatlands dominate global natural methane emissions (2, 4, 9–12, 14, 17, 25, 79–87). Our data provide additional support for this hypothesis. To underscore the tropical (Ax) or wet and warm temperate (Cax) climatic boundary conditions (where x denotes any of the second characters of the classical Köppen–Geiger climate classification in table 1 of ref. 88, necessary for such wetlands), we refer to this group of methane-emitting systems as AxCax wetlands throughout. The AxCax wetlands are largely located in regions influenced by seasonal swings of the ITCZ (17, 89–95). Because the sizes of AxCax regions are not evenly distributed in both hemispheres, a good portion of their emissions (located, for example, in Southeast Asia) also contributes to the IPD in methane mixing ratio over a wide range of climate states (9).

Temperature, precipitation, the water table, and net primary production (NPP) are regarded to be the main factors controlling CH_4 fluxes in AxCax wetlands (80, 92, 96, 97). Low $[CO_2]$ during glacials reduces NPP (98), and we expect decreased fluxes from AxCax wetlands as a direct consequence. However, lower glacial sea level led to newly exposed AxCax landmasses (such as the Sunda Shelf), where wetlands could develop (16). On top of an overall reduction in AxCax CH_4 fluxes during glacial times, substantial ecosystem shifts leading to a larger C4/C3 plant ratio may explain parts of the glacial $\delta^{13}CH_4$ evolution (ref. 25 and references therein).

Specific evidence for the key role of AxCax wetland CH_4 emissions comes from the rather small amplitudes in the $\delta D(CH_4)$ response for stadial/interstadial (36) and glacial/interglacial changes (Fig. 1 and Table S1) (31). Because extratropical methane sources have a stronger leverage on the integrated hydrogen isotopic source signature, they are expected to experience larger glacial/interglacial $\delta D(CH_4)$ changes than their AxCax counterparts. Records from speleothems (85, 99) and plant waxes (100) located in AxCax climates suggest amplitudes for (meteoric) waters used for methanogenesis that are in line with our atmospheric $\delta D(CH_4)$ data (Fig. 1). High-latitude changes in δD of precipitation are much stronger (35, 101) and would lead to $\delta D(CH_4)$ changes too large compared with our data if this source were to control the observed CH_4 variations.

The earlier proposal by Ridgwell et al. (102) that flooding of the continental shelves is a main contributor to initial steep methane rises is in line with our dual isotope records.

Apart from the overall glacial/interglacial shifts, the variations in $\delta^{13}CH_4$ are largely decoupled from the changes in $\delta D(CH_4)$. To understand the observed variations in $\delta^{13}CH_4$ (Fig. 1), we discuss in the following changes on the Indonesian archipelago, a region for which wetland history since the LGM has been studied in great detail and that can, therefore, serve as a blueprint for our process understanding. Recently, Dommain et al. (103) presented local sea level as the key player controlling Sundaland's wetland extent since the LGM. Rising sea level during the deglaciation and Early Holocene lowers the regional hydraulic gradient, leading to higher water tables for peatlands in this region. Falling local sea levels after 5 ka BP lead to an expansion of peatlands located in the coastal lowlands (103). Furthermore, sea-level changes in the Sunda Shelf region may also control moisture supply in the Indo-Pacific Warm Pool and intensity of monsoonal rainfall (85, 99, 104, 105). Taken together, these findings suggest that AxCax wetland CH_4 emissions from the Indonesian archipelago may vary over precessional timescales because of sea level and precipitation changes. We note that Sundaland represents only a fraction of tropical wetland area, and we suggest that other large-scale tropical methane-emitting systems (like the Amazon and the Congo basins) responded similarly to (local) sea level and hence, hydrological gradient changes. Taken together, wetland methane emissions of South America, Africa, and Sundaland can explain the observed ice core signals.

Dommain et al. (103) also suggest that the exposure of the Sunda Shelf led to drier conditions after MIS 3, causing degraded inland wetlands during the LGM. We propose that the baseline level of atmospheric methane (2, 106) is in fact determined by AxCax wetlands (located in Sundaland and other AxCax regions) and that its decline to the lowest levels observed in ice cores after MIS 3 is caused by the drying of tropical wetland systems. We observe that the CH_4 response reported for Greenland interstadials (DO 2/3, 18/19/20, and 22/23) during periods of falling sea level is generally small (8, 107, 108). In other words, $[CH_4]$ only shows large stadial/interstadial increases during periods of rising (local) sea level when insolation and increased monsoon precipitation could, in principle, boost wetland CH_4 emissions (2, 4, 19, 25, 70, 106, 109). Hence, only under the prerequisite of a low(ering) hydraulic gradient in AxCax wetland regions can any forcing (temperature or precipitation) lead to strong methane production increases during DO events and glacial/interglacial terminations.

One open question remaining is why MIS 5.5 and MIS 11.3 $[CH_4]$ and $\delta^{13}CH_4$ histories differ drastically in their temporal evolution, whereas $\delta D(CH_4)$ is rather constant: near −89‰ for both interglacials (Fig. 1). Most importantly, a pronounced minimum in $\delta^{13}CH_4$ is found at the end of MIS 5.5 (116 ka BP) during the time of minimal northern insolation. At the same

time, [CH_4] decreases continuously toward glacial levels, with a steeper decrease from the minimum $\delta^{13}CH_4$ values onward. The following scenarios cannot be used to explain the $\delta^{13}CH_4$ minimum during MIS 5.5. (*i*) A proportional reduction of all sources. Because this scenario would lead to no signal in $\delta^{13}CH_4$, it can be ruled out. Thus, a change in the source mix or a shift in the isotopic signature of the (dominant) source(s) is required. (*ii*) Reduced microbial emissions while keeping geologic and BB emissions constant. Because this combination would produce higher $\delta^{13}CH_4$ when total CH_4 decreases, it also cannot explain our observations. (*iii*) Stable or even increasing emissions from microbial, isotopically light sources [such as ^{13}C- and D-depleted (boreal) wetlands and thermokarst, permafrost]. This setting would call for overcompensation by decreasing ^{13}C-enriched emissions to meet falling [CH_4]. Accordingly, decreasing emissions from BB and/or GEM could result in the observed low $\delta^{13}CH_4$ values. The last two scenarios can be ruled out on the basis of our $\delta D(CH_4)$ constraint, because we would expect coevolving trends for both isotopes. In contrast, our $\delta D(CH_4)$ data show no clear trend during this time period.

The $\delta^{13}CH_4$ minimum occurs at the very end of MIS 5.5 at a time when $\delta^{15}N_2$ and [CO_2] indicate the end of the warm period (Fig. S3) (50, 51, 110). At that time, [CH_4] is already close to glacial levels of below 500 ppb (4). We propose that the lowest interglacial CH_4 levels (coincident with northern insolation minima at the start and end of MIS 11.3, the end of MIS 5.5, and the mid Holocene) are also mainly because of decreased AxCax wetland emissions. At the same time, these periods are connected to $\delta^{13}CH_4$ minima. To close the isotope budget, a simultaneous reduction in a relatively ^{13}C-enriched source is required. Hence, additionally, declining BB emissions are proposed to meet all constraints. Such a scenario is in line with lower BB emissions under cooling climate conditions (24) and recently published speleothem data (70) showing reduced Asian monsoon strength corresponding to low [CH_4] and low $\delta^{13}CH_4$ during MIS 11.3 and for the late MIS 5.5 $\delta^{13}CH_4$ minimum.

Interestingly, CH_4 and $\delta^{13}CH_4$ decrease during the first one-half of the Holocene but reverse their trend during the second one-half, when northern insolation is still declining. To explain this feature, Ruddiman (77) proposed an early human influence. An alternative scenario meeting all of the constraints presented is that of stronger southern insolation, leading to increasing CH_4 emissions of AxCax wetlands in the tropical Southern Hemisphere (e.g., South America). This scenario is consistent with proxy data (111, 112) and a CH_4/climate model study (78). Moreover, our CH_4 and $\delta^{13}CH_4$ data during MIS 11.3 show the same behavior as in the Holocene. We can conclude that the Holocene trends operate similarly to MIS 11.3, with strong southern insolation causing increased southern tropical AxCax wetland emissions during the last 5 ka. For MIS 5.5, this insolation boost from the south would have come too late and already during falling sea level, causing [CH_4] to drop continuously.

In summary, we conclude that tropical methane-emitting systems are the key players among all natural methane emitters, reflecting changes in (local) sea level, monsoon strength, and temperature induced by orbital changes.

Biome and Fire Regime Changes Caused by Megafauna Extinction. Arguably, the most surprising feature of our records (Fig. 1) is the pronounced difference in absolute levels for both $\delta^{13}CH_4$ and $\delta D(CH_4)$ for the Holocene compared with MIS 5.5 and MIS 11.3 and for the LGM compared with MIS 6 and MIS 12. Shifts of ~2–3‰ for $\delta^{13}CH_4$ and 10–18‰ for $\delta D(CH_4)$ toward higher numbers are found, with no obvious difference in CH_4 mixing ratio between these time slices (Table S1) (42). Straightforward explanations for similar [CH_4] accompanied by shifted isotope records require changes in the source signatures or changes in emission strength of a source with strong leverage. To our knowledge, no general isotope shifts of that size have been described in precursor materials for methanogenesis before MIS 2. It is also unlikely that the source strength or signature of GEM or biogenic emissions changed markedly compared with previous glacial/interglacial cycles. In fact, GEM is expected to change in response to sea level or ice sheet extent, but the two parameters remain within a similar range for all glacials and all interstadials considered in this study. One possibility to reconcile the observations is CH_4 emission changes related to changes in biomes and fire regimes, because BB is a CH_4 source strongly enriched in ^{13}C and D (13, 22, 65). BB is an ancient and persistent feature throughout the geologic record (113), and there is evidence of net changes in fire regimes as a consequence of the megafauna extinction that was presumably caused by rapid climate changes in combination with human interference in the course of the last glacial (refs. 114–119 and references therein). The review by Johnson (120) on the timing of the arrival of humans on different continents and the ecological consequences of megafauna extinction supports the idea that increased fire frequency was caused by increased vegetation density and the accumulation of plant material not consumed by herbivores. For example, records from Australia of charcoal, different plant pollen types, and spores of the fungus *Sporormiella* are used by Rule et al. (121) to indicate large herbivore activity and conclude that megafauna extinction caused increased fire activity after 41 ka BP. Furthermore, these Australian records show that fires were common during the Holocene but much less frequent in the previous interglacial. We note that responses might be different in other parts of the globe (122–124) and that, today, Australia accounts for only roughly 6% of global fire carbon emissions (125). However, other authors reported similar observations of fire activity changes on other continents (126, 127), but a global synthesis is not available yet.

Assuming similar GEM for all of the time periods investigated, we can derive the net change in BB emissions for different time periods from Fig. 2, where we compare model interglacial (glacial) runs with the same interglacial (glacial) model parameters (all identical except for a small shift from the microbial source to BB). For example, an assumption of 30 Tg CH_4 a^{-1} of GEM results in a shift in BB emissions for the Holocene by 15 Tg CH_4 a^{-1} (or +83%) compared with MIS 5.5 and MIS 11.3. For the LGM, the model results show an increase in BB emissions by about 7 Tg CH_4 a^{-1} (or +54%) compared with MIS 6 and 3 Tg CH_4 a^{-1} (or +18%) compared with MIS 12. Hence, our dual stable isotope records (Fig. 1) directly support the hypothesis (120, 121) of higher fire activity during the Holocene and the LGM compared with previous interglacials and glacials, respectively. At the same time, the largely unchanged CH_4 levels suggest that direct CH_4 emissions from large animals are confined to the lower end of values found in the literature (128).

Conclusions

Stable isotopic methane records from polar ice cores offer insights into past methane emission inventories and significantly improve our quantitative understanding of past atmospheric methane changes. With our dual isotope data, we can rule out a dominant role for GEM in the glacial methane budget and especially, past emission changes. In fact, methane emissions from tropical wetland and seasonally inundated floodplain systems seem to be the strongest source for not only interglacials but also, glacials. These emissions play the major role in the waxing and waning of atmospheric methane mixing ratios recorded in polar ice. Key parameters to control CH_4 emissions in these wetland systems (AxCax wetlands) are temperature and the water table as steered by a combination of solar insolation, (local) sea level, and monsoon strength. Between 80 and 25 ka BP, the CH_4 emissions experienced a shift in both stable isotopes, leading to higher (heavier) values for the younger part. This observation is hard to explain by climate-driven wetland changes. We propose that this shift is caused by biome changes that foster

BB emissions in the course of the late Quaternary megafauna extinction.

Materials and Methods

$\delta^{13}CH_4$ Analysis of Ice Core Samples. All presented $\delta^{13}CH_4$ data were measured at the University of Bern using the system described in detail in ref. 47. All data are free of a krypton interference (48). Blank ice measurements indicate no artifacts associated with ice processing (47). The external precision (1-sigma SD) is estimated based on the long-term repeatability of replicate ice core analyses to be better than 0.15‰ (47). Our reference is a bottle of Pacific air calibrated at the Stable Isotope Laboratory of the Institute of Arctic and Alpine Research (University of Colorado) (47). All $\delta^{13}CH_4$ data are given using the δ notation on the VPDB scale. $\delta^{13}CH_4$ data have been corrected for gravitational settling in the firn using published $\delta^{15}N_2$ records (*SI Text*). In polar firn, diffusive isotopic fractionation takes place when large and rapid changes of the CH_4 mixing ratio (129, 130) occur. We calculated the expected influence of this effect according to the procedure presented in ref. 129 and apply this correction to the data plotted in our figures. Note that these effects are rather short-lived and very small for our selected samples and do not affect any of our conclusions. [CH_4] data shown in our figures were obtained using the isotope analysis and have an estimated 1-sigma error of 5 ppb based on TALDICE replicate measurements (47).

$\delta D(CH_4)$ Analysis of Ice Core Samples. All presented $\delta D(CH_4)$ data have been measured at the University of Bern using the system described in detail in ref. 46. All data are free of a krypton interference. Blank ice measurements indicate no artifacts associated with ice processing (131). For $\delta D(CH_4)$, the external precision (used as error bars in the figures) is estimated based on the 1-sigma SD of our daily standard gas measurements used to calibrate the sample. This uncertainty ranged between 0.9‰ and 3.8‰, with a median of 2.1‰. Replicate analyses of ice core samples indicate a reproducibility of better than 2.3‰ (pooled 1-sigma SD for measurements performed during a time period of 3.5 y) (46). All data are given in the commonly used δ notation on the VSMOW scale. Note that no international reference standard for $\delta D(CH_4)$ in air/ice core samples exists so far. Our data are tied to the scale of the Institute for Environmental Physics in Heidelberg, Germany using a cross-calibrated bottle of recent air (46). A laboratory offset to measurements from the United States is evident (46). $\delta D(CH_4)$ data have been corrected for gravitational settling in the firn using published $\delta^{15}N_2$ records (*SI Text*). No corrections concerning diffusive isotopic fractionation (129, 130) have been performed for $\delta D(CH_4)$ data (*SI Text*), because the size of this correction is negligible compared with the $\delta D(CH_4)$ variations.

Box Model. We used the box model presented in refs. 32 and 36 to assess maximal GEM and increased emissions by BB for the last 25 ka compared with previous time periods. The atmosphere of the model consists of four boxes (northern and southern troposphere and stratosphere) with prescribed air mass exchange. CH_4 emissions into the tropospheric boxes as well as their source signatures and sink fractions are varied in a Monte Carlo approach. The model is run into steady state, and the equilibrium value of the southern troposphere box is compared with the data constraints (Table S1). If the modeled [CH_4], $\delta^{13}CH_4$, and $\delta D(CH_4)$ values are compatible [within the uncertainty of the measured data (Table S1)], the input values are recorded as a possible CH_4 budget solution. For each time slice, 10,000 valid runs are collected. To be consistent with work on the recent methane budget (63), we distinguish only three source categories here: GEM, BB, and a microbial source including natural emissions by wetlands, ruminants, and termites. Isotopic signatures of the sources are based partly on our previous work (refs. 32 and 36 and references therein) and mainly on the collection by Schwietzke et al. (63) with some modifications (details are in *SI Text* and Table S2). In particular, we adjusted the geographical distribution of the sources to be consistent with IPD estimates for [CH_4] (9, 79, 89, 132) and lowered the isotopic signature of the Northern Hemisphere microbial source. To account for biome shifts during the glacial, we shift the microbial and BB source signatures by +2.6‰ in line with the interpretation given in ref. 25. The model uses four sinks (tropospheric OH, stratospheric loss, soils, and tropospheric Cl), with fractions that have been varied according to Table S3. Overall, our atmospheric isotope constraints are free of a methodologically caused krypton artifact perturbing previous studies, leading to generally lower $\delta^{13}CH_4$ constraints and hence, lower GEM/BB estimates in our study.

ACKNOWLEDGMENTS. We thank Sepp Kipfstuhl and the Alfred Wegener Institute (AWI) for providing EDML samples from MIS 5.5. We also thank Gregory Teste (IGE) for help in sample cutting. Anne-Laure Daniau, Jennifer Marlon, and Cathy Whitlock are acknowledged for helpful inputs on fire histories. We thank two reviewers for their valuable comments. Primary logistical support was provided by Programma Nazionale di Ricerche in Antartide (PNRA) at Talos Dome. The collaborative research on the Vostok ice core was carried out in the frame of the Russian–French International Associated Laboratory Climate and Environments from Ice Archives. The research leading to these results has received funding from the European Research Council (ERC) under the European Union's Seventh Framework Programme FP7/2007-2013 ERC Grant 226172 [ERC Advanced Grant Modern Approaches to Temperature Reconstructions in Polar Ice Cores (MATRICs)] and the Swiss National Science Foundation. This work is a contribution to EPICA, a joint European Science Foundation/European Commission scientific program funded by the European Union and national contributions from Belgium, Denmark, France, Germany, Italy, The Netherlands, Norway, Sweden, Switzerland, and the United Kingdom. The main logistic support was provided by Institut Polaire Français Paul-Emile Victor (IPEV) and PNRA (at Dome C) and AWI (at EDML). TALDICE, a joint European program, is funded by national contributions from Italy, France, Germany, Switzerland, and the United Kingdom. This work is EPICA publication no. 306 and TALDICE publication no. 45.

1. Dlugokencky EJ, Steele LP, Lang PM, Masarie KA (1995) Atmospheric methane at Mauna-Loa and Barrow Observatories: Presentation and analysis of in-situ measurements. *J Geophys Res Atmos* 100:23103–23113.
2. Brook EJ, Sowers T, Orchardo J (1996) Rapid variations in atmospheric methane concentration during the past 110,000 years. *Science* 273:1087–1091.
3. Bousquet P, et al. (2006) Contribution of anthropogenic and natural sources to atmospheric methane variability. *Nature* 443:439–443.
4. Loulergue L, et al. (2008) Orbital and millennial-scale features of atmospheric CH_4 over the past 800,000 years. *Nature* 453:383–386.
5. Mitchell LE, Brook EJ, Sowers T, McConnell JR, Taylor K (2011) Multidecadal variability of atmospheric methane, 1000–1800 CE. *J Geophys Res Biogeosci* 116:G02007.
6. Etheridge DM, Steele LP, Francey RJ, Langenfelds RL (1998) Atmospheric methane between 1000 AD and present: Evidence of anthropogenic emissions and climatic variability. *J Geophys Res Atmos* 103:15979–15993.
7. MacFarling Meure C, et al. (2006) Law Dome CO_2, CH_4 and N_2O ice core records extended to 2000 years BP. *Geophys Res Lett* 33:1–4.
8. Baumgartner M, et al. (2014) NGRIP CH_4 concentration from 120 to 10 kyr before present and its relation to a $\delta^{15}N$ temperature reconstruction from the same ice core. *Clim Past* 10:903–920.
9. Baumgartner M, et al. (2012) High-resolution interpolar difference of atmospheric methane around the Last Glacial Maximum. *Biogeosciences* 9:3961–3977.
10. Kirschke S, et al. (2013) Three decades of global methane sources and sinks. *Nat Geosci* 6:813–823.
11. Saunois M, et al. (2016) The global methane budget 2000–2012. *Earth Syst Sci Data* 8:697–751.
12. Nisbet EG, et al. (2016) Rising atmospheric methane: 2007–2014 Growth and isotopic shift. *Global Biogeochem Cycles* 30:1356–1370.
13. Quay P, et al. (1999) The isotopic composition of atmospheric methane. *Global Biogeochem Cycles* 13:445–461.
14. Bousquet P, et al. (2011) Source attribution of the changes in atmospheric methane for 2006–2008. *Atmos Chem Phys* 11:3689–3700.
15. Schaefer H, et al. (2016) A 21st-century shift from fossil-fuel to biogenic methane emissions indicated by $^{13}CH_4$. *Science* 352:80–84.
16. Kaplan JO (2002) Wetlands at the Last Glacial Maximum: Distribution and methane emissions. *Geophys Res Lett* 29:1079.
17. Rhodes RH, et al. (2015) Paleoclimate. Enhanced tropical methane production in response to iceberg discharge in the North Atlantic. *Science* 348:1016–1019.
18. Guo ZT, Zhou X, Wu HB (2012) Glacial-interglacial water cycle, global monsoon and atmospheric methane changes. *Clim Dyn* 39:1073–1092.
19. Wang PX, et al. (2014) The global monsoon across timescales: Coherent variability of regional monsoons. *Clim Past* 10:2007–2052.
20. Walter KM, Edwards ME, Grosse G, Zimov SA, Chapin FS, 3rd (2007) Thermokarst lakes as a source of atmospheric CH_4 during the last deglaciation. *Science* 318:633–636.
21. Anthony KMW, Anthony P, Grosse G, Chanton J (2012) Geologic methane seeps along boundaries of Arctic permafrost thaw and melting glaciers. *Nat Geosci* 5:419–426.
22. Snover AK, Quay PD, Hao WM (2000) The D/H content of methane emitted from biomass burning. *Global Biogeochem Cycles* 14:11–24.
23. Power MJ, et al. (2008) Changes in fire regimes since the Last Glacial Maximum: An assessment based on a global synthesis and analysis of charcoal data. *Clim Dyn* 30:887–907.
24. Daniau AL, et al. (2012) Predictability of biomass burning in response to climate changes. *Global Biogeochem Cycles* 26:GB4007.
25. Möller L, et al. (2013) Independent variations of CH_4 emissions and isotopic composition over the past 160,000 years. *Nat Geosci* 6:885–890.
26. Marlon JR, et al. (2016) Reconstructions of biomass burning from sediment-charcoal records to improve data-model comparisons. *Biogeosciences* 13:3225–3244.
27. Etiope G, Klusman RW (2002) Geologic emissions of methane to the atmosphere. *Chemosphere* 49:777–789.

28. Etiope G, Lassey KR, Klusman RW, Boschi E (2008) Reappraisal of the fossil methane budget and related emission from geologic sources. *Geophys Res Lett* 35:L09307.
29. Etiope G, Milkov AV, Derbyshire E (2008) Did geologic emissions of methane play any role in Quaternary climate change? *Global Planet Change* 61:79–88.
30. Ferretti DF, et al. (2005) Unexpected changes to the global methane budget over the past 2000 years. *Science* 309:1714–1717.
31. Sowers T (2006) Late Quaternary atmospheric CH_4 isotope record suggests marine clathrates are stable. *Science* 311:838–840.
32. Fischer H, et al. (2008) Changing boreal methane sources and constant biomass burning during the last termination. *Nature* 452:864–867.
33. Petrenko VV, et al. (2009) $^{14}CH_4$ measurements in Greenland ice: Investigating last glacial termination CH_4 sources. *Science* 324:506–508.
34. Schaefer H, Whiticar MJ (2008) Potential glacial-interglacial changes in stable carbon isotope ratios of methane sources and sink fractionation. *Global Biogeochem Cycles* 22:GB1001.
35. Waldron S, Lansdown JM, Scott EM, Fallick AE, Hall AJ (1999) The global influence of the hydrogen isotope composition of water on that of bacteriogenic methane from shallow freshwater environments. *Geochim Cosmochim Acta* 63:2237–2245.
36. Bock M, et al. (2010) Hydrogen isotopes preclude marine hydrate CH_4 emissions at the onset of Dansgaard-Oeschger events. *Science* 328:1686–1689.
37. Brosius LS, et al. (2012) Using the deuterium isotope composition of permafrost meltwater to constrain thermokarst lake contributions to atmospheric CH_4 during the last deglaciation. *J Geophys Res Biogeosci* 117:G01022.
38. Rice AL, et al. (2016) Atmospheric methane isotopic record favors fossil sources flat in 1980s and 1990s with recent increase. *Proc Natl Acad Sci USA* 113:10791–10796.
39. Whiticar MJ, Faber E (1986) Methane oxidation in sediment and water column environments—Isotope evidence. *Org Geochem* 10:759–768.
40. Levine JG, Wolff EW, Hopcroft PO, Valdes PJ (2012) Controls on the tropospheric oxidizing capacity during an idealized Dansgaard-Oeschger event, and their implications for the rapid rises in atmospheric methane during the last glacial period. *Geophys Res Lett* 39:L12805.
41. Murray LT, et al. (2014) Factors controlling variability in the oxidative capacity of the troposphere since the Last Glacial Maximum. *Atmos Chem Phys* 14:3589–3622.
42. Quiquet A, et al. (2015) The relative importance of methane sources and sinks over the Last Interglacial period and into the last glaciation. *Quat Sci Rev* 112:1–16.
43. Hopcroft PO, Valdes PJ, O'Connor FM, Kaplan JO, Beerling DJ (2017) Understanding the glacial methane cycle. *Nat Commun* 8:14383.
44. Martinson DG, et al. (1987) Age dating and the orbital theory of the ice ages: Development of a high-resolution 0 to 300,000-year chronostratigraphy. *Quat Res* 27: 1–29.
45. Lisiecki LE, Raymo ME (2005) A Pliocene-Pleistocene stack of 57 globally distributed benthic δ18O records. *Paleoceanography* 20:PA1003.
46. Bock M, Schmitt J, Beck J, Schneider R, Fischer H (2014) Improving accuracy and precision of ice core $\delta D(CH_4)$ analyses using methane pre-pyrolysis and hydrogen post-pyrolysis trapping and subsequent chromatographic separation. *Atmos Meas Tech* 7:1999–2012.
47. Schmitt J, Seth B, Bock M, Fischer H (2014) Online technique for isotope and mixing ratios of CH_4, N_2O, Xe and mixing ratios of organic trace gases on a single ice core sample. *Atmos Meas Tech* 7:2645–2665.
48. Schmitt J, et al. (2013) On the interference of Kr during carbon isotope analysis of methane using continuous-flow combustion–isotope ratio mass spectrometry. *Atmos Meas Tech* 6:1425–1445.
49. Sowers T (2010) Atmospheric methane isotope records covering the Holocene period. *Quat Sci Rev* 29:213–221.
50. Schneider R, Schmitt J, Köhler P, Joos F, Fischer H (2013) A reconstruction of atmospheric carbon dioxide and its stable carbon isotopic composition from the penultimate glacial maximum to the last glacial inception. *Clim Past* 9:2507–2523.
51. Landais A, et al. (2013) Two-phase change in CO_2, Antarctic temperature and global climate during Termination II. *Nat Geosci* 6:1062–1065.
52. Kennett JP, Cannariato KG, Hendy IL, Behl RJ (2003) *Methane Hydrates in Quaternary Climate Change: The Clathrate Gun Hypothesis* (American Geophysical Union, Washington, DC).
53. de Garidel-Thoron T, Beaufort L, Bassinot F, Henry P (2004) Evidence for large methane releases to the atmosphere from deep-sea gas-hydrate dissociation during the last glacial episode. *Proc Natl Acad Sci USA* 101:9187–9192.
54. Judd AG, Hovland M, Dimitrov LI, Garcia-Gil S, Jukes V (2002) The geological methane budget at Continental Margins and its influence on climate change. *Geofluids* 2:109–126.
55. Shakhova N, et al. (2010) Extensive methane venting to the atmosphere from sediments of the East Siberian Arctic Shelf. *Science* 327:1246–1250.
56. Fisher RE, et al. (2011) Arctic methane sources: Isotopic evidence for atmospheric inputs. *Geophys Res Lett* 38:L21803.
57. Berchet A, et al. (2016) Atmospheric constraints on the methane emissions from the East Siberian Shelf. *Atmos Chem Phys* 16:4147–4157.
58. Myhre CL, et al. (2016) Extensive release of methane from Arctic seabed west of Svalbard during summer 2014 does not influence the atmosphere. *Geophys Res Lett* 43:4624–4631.
59. Shakhova N, et al. (2010) Geochemical and geophysical evidence of methane release over the East Siberian Arctic Shelf. *J Geophys Res Oceans* 115:C08007.
60. Nisbet EG (2002) Have sudden large releases of methane from geological reservoirs occurred since the Last Glacial Maximum, and could such releases occur again? *Philos Trans A Math Phys Eng Sci* 360:581–607.
61. Luyendyk B, Kennett J, Clark JF (2005) Hypothesis for increased atmospheric methane input from hydrocarbon seeps on exposed continental shelves during glacial low sea level. *Mar Pet Geol* 22:591–596.
62. Petrenko VVS, et al. (2014) New measurements of 14C provide constraints on sources of a large atmospheric methane increase during the Younger Dryas–Preboreal abrupt warming event. *Proceedings of the American Geophysical Union Fall Meeting 2014* (American Geophysical Union, Washington, DC).
63. Schwietzke S, et al. (2016) Upward revision of global fossil fuel methane emissions based on isotope database. *Nature* 538:88–91.
64. Sapart CJ, et al. (2012) Natural and anthropogenic variations in methane sources during the past two millennia. *Nature* 490:85–88.
65. Dlugokencky EJ, Nisbet EG, Fisher R, Lowry D (2011) Global atmospheric methane: Budget, changes and dangers. *Philos Trans A Math Phys Eng Sci* 369:2058–2072.
66. Dalsøren SB, et al. (2016) Atmospheric methane evolution the last 40 years. *Atmos Chem Phys* 16:3099–3126.
67. Köhler P, Knorr G, Bard E (2014) Permafrost thawing as a possible source of abrupt carbon release at the onset of the Bølling/Allerød. *Nat Commun* 5:5520.
68. Melton JR, Schaefer H, Whiticar MJ (2012) Enrichment in ^{13}C of atmospheric CH_4 during the Younger Dryas termination. *Clim Past* 8:1177–1197.
69. Sriskantharajah S, et al. (2012) Stable carbon isotope signatures of methane from a Finnish subarctic wetland. *Tellus B* 64:18818.
70. Cheng H, et al. (2016) The Asian monsoon over the past 640,000 years and ice age terminations. *Nature* 534:640–646.
71. Frolking S, Roulet NT (2007) Holocene radiative forcing impact of northern peatland carbon accumulation and methane emissions. *Glob Chang Biol* 13:1079–1088.
72. Korhola A, et al. (2010) The importance of northern peatland expansion to the late-Holocene rise of atmospheric methane. *Quat Sci Rev* 29:611–617.
73. Yu ZC, et al. (2013) Evidence for elevated emissions from high-latitude wetlands contributing to high atmospheric CH_4 concentration in the early Holocene. *Global Biogeochem Cycles* 27:131–140.
74. Alstad KP, Whiticar MJ (2011) Carbon and hydrogen isotope ratio characterization of methane dynamics for Fluxnet Peatland Ecosystems. *Org Geochem* 42:548–558.
75. Hornibrook ERC (2013) The stable carbon isotope composition of methane produced and emitted from Northern Peatlands. *Carbon Cycling in Northern Peatlands*, eds Baird AJ, Belyea LR, Comas X, Reeve AS, Slater LD (American Geophysical Union, Washington, DC), pp 187–203.
76. Le Mer J, Roger P (2001) Production, oxidation, emission and consumption of methane by soils: A review. *Eur J Soil Biol* 37:25–50.
77. Ruddiman WF (2003) The anthropogenic greenhouse era began thousands of years ago. *Clim Change* 61:261–293.
78. Singarayer JS, Valdes PJ, Friedlingstein P, Nelson S, Beerling DJ (2011) Late Holocene methane rise caused by orbitally controlled increase in tropical sources. *Nature* 470: 82–85.
79. Mitchell L, Brook E, Lee JE, Buizert C, Sowers T (2013) Constraints on the late holocene anthropogenic contribution to the atmospheric methane budget. *Science* 342:964–966.
80. Fung I, et al. (1991) Three-dimensional model synthesis of the global methane cycle. *J Geophys Res Atmos* 96:13033–13065.
81. Chappellaz J, Barnola J, Raynaud D, Korotkevich YS, Lorius C (1990) Ice-core record of atmospheric methane over the past 160,000 years. *Nature* 345:127–131.
82. Raynaud D, et al. (1993) The ice core record of greenhouse gases. *Science* 259: 926–934.
83. Chappellaz J, et al. (1993) Synchronous changes in atmospheric CH_4 and Greenland climate between 40 and 8 kyr BP. *Nature* 366:443–445.
84. Severinghaus JP, Beaudette R, Headly MA, Taylor K, Brook EJ (2009) Oxygen-18 of O_2 records the impact of abrupt climate change on the terrestrial biosphere. *Science* 324:1431–1434.
85. Griffiths ML, et al. (2009) Increasing Australian-Indonesian monsoon rainfall linked to early Holocene sea-level rise. *Nat Geosci* 2:636–639.
86. Frankenberg C, et al. (2008) Tropical methane emissions: A revised view from SCIAMACHY onboard ENVISAT. *Geophys Res Lett* 35:L15811.
87. Sperlich P, et al. (2015) Carbon isotope ratios suggest no additional methane from boreal wetlands during the rapid Greenland Interstadial 21.2. *Global Biogeochem Cycles* 29:1962–1976.
88. Peel MC, Finlayson BL, McMahon TA (2007) Updated world map of the Koppen-Geiger climate classification. *Hydrol Earth Syst Sci* 11:1633–1644.
89. Brook EJ, Harder S, Severinghaus J, Steig EJ, Sucher CM (2000) On the origin and timing of rapid changes in atmospheric methane during the last glacial period. *Global Biogeochem Cycles* 14:559–572.
90. Wang YJ, et al. (2001) A high-resolution absolute-dated late Pleistocene Monsoon record from Hulu Cave, China. *Science* 294:2345–2348.
91. Wang X, et al. (2004) Wet periods in northeastern Brazil over the past 210 kyr linked to distant climate anomalies. *Nature* 432:740–743.
92. Bloom AA, Palmer PI, Fraser A, Reay DS, Frankenberg C (2010) Large-scale controls of methanogenesis inferred from methane and gravity spaceborne data. *Science* 327: 322–325.
93. Matthews E, Fung I (1987) Methane emission from natural wetlands: Global distribution, area and environmental characteristics of sources. *Global Biogeochem Cycles* 1:61–67.
94. Matthews E (1993) Wetlands. *Atmospheric Methane: Sources, Sinks, and Role in Global Change*, ed Khalil MAK (Springer, Berlin), pp 314–361.
95. Prigent C, Aires F, Rossow W, Matthews E (2001) Joint characterization of vegetation by satellite observations from visible to microwave wavelengths: A sensitivity analysis. *J Geophys Res Atmos* 106:20665–20685.

96. Whiting GJ, Chanton JP (1993) Primary production control of methane emission from wetlands. *Nature* 364:794–795.
97. Burns SJ (2011) Speleothem records of changes in tropical hydrology over the Holocene and possible implications for atmospheric methane. *Holocene* 21:735–741.
98. Gerhart LM, Ward JK (2010) Plant responses to low [CO_2] of the past. *New Phytol* 188:674–695.
99. Griffiths ML, et al. (2010) Younger Dryas–Holocene temperature and rainfall history of southern Indonesia from $\delta^{18}O$ in speleothem calcite and fluid inclusions. *Earth Planet Sci Lett* 295:30–36.
100. Shanahan TM, et al. (2015) The time-transgressive termination of the African Humid Period. *Nat Geosci* 8:140–144.
101. Bowen GJ, Wilkinson B (2002) Spatial distribution of delta O-18 in meteoric precipitation. *Geology* 30:315–318.
102. Ridgwell A, Maslin M, Kaplan JO (2012) Flooding of the continental shelves as a contributor to deglacial CH_4 rise. *J Quat Sci* 27:800–806.
103. Dommain R, et al. (2014) Carbon storage and release in Indonesian peatlands since the last deglaciation. *Quat Sci Rev* 97:1–32.
104. DiNezio PN, Tierney JE (2013) The effect of sea level on glacial Indo-Pacific climate. *Nat Geosci* 6:485–491.
105. Meckler AN, Clarkson MO, Cobb KM, Sodemann H, Adkins JF (2012) Interglacial hydroclimate in the tropical West Pacific through the Late Pleistocene. *Science* 336: 1301–1304.
106. Flückiger J, et al. (2004) N_2O and CH_4 variations during the last glacial epoch: Insight into global processes. *Global Biogeochem Cycles* 18:GB1020.
107. Chappellaz J, et al. (2013) High-resolution glacial and deglacial record of atmospheric methane by continuous-flow and laser spectrometer analysis along the NEEM ice core. *Clim Past* 9:2579–2593.
108. Grant KM, et al. (2014) Sea-level variability over five glacial cycles. *Nat Commun* 5:5076.
109. Wang Y, et al. (2008) Millennial- and orbital-scale changes in the East Asian monsoon over the past 224,000 years. *Nature* 451:1090–1093.
110. Bereiter B, et al. (2015) Revision of the EPICA Dome C CO_2 record from 800 to 600 kyr before present. *Geophys Res Lett* 42:542–549.
111. Haug GH, Hughen KA, Sigman DM, Peterson LC, Röhl U (2001) Southward migration of the intertropical convergence zone through the Holocene. *Science* 293:1304–1308.
112. van Breukelen MR, Vonhof HB, Hellstrom JC, Wester WCG, Kroon D (2008) Fossil dripwater in stalagmites reveals Holocene temperature and rainfall variation in Amazonia. *Earth Planet Sci Lett* 275:54–60.
113. Bird MI, Cali JA (1998) A million-year record of fire in sub-Saharan Africa. *Nature* 394:767–769.
114. Cooper A, et al. (2015) PALEOECOLOGY. Abrupt warming events drove Late Pleistocene Holarctic megafaunal turnover. *Science* 349:602–606.
115. Bartlett LJ, et al. (2016) Robustness despite uncertainty: Regional climate data reveal the dominant role of humans in explaining global extinctions of Late Quaternary megafauna. *Ecography (Cop.)* 39:152–161.
116. Villavicencio NA, et al. (2016) Combination of humans, climate, and vegetation change triggered Late Quaternary megafauna extinction in the ultima Esperanza region, southern Patagonia, Chile. *Ecography (Cop.)* 39:125–140.
117. Malhi Y, et al. (2016) Megafauna and ecosystem function from the Pleistocene to the Anthropocene. *Proc Natl Acad Sci USA* 113:838–846.
118. Bakker ES, et al. (2016) Combining paleo-data and modern exclosure experiments to assess the impact of megafauna extinctions on woody vegetation. *Proc Natl Acad Sci USA* 113:847–855.
119. van der Kaars S, et al. (2017) Humans rather than climate the primary cause of Pleistocene megafaunal extinction in Australia. *Nat Commun* 8:14142.
120. Johnson CN (2009) Ecological consequences of Late Quaternary extinctions of megafauna. *Proc R Soc Lond B Biol Sci* 276:2509–2519.
121. Rule S, et al. (2012) The aftermath of megafaunal extinction: Ecosystem transformation in Pleistocene Australia. *Science* 335:1483–1486.
122. Barnosky AD, et al. (2016) Variable impact of late-Quaternary megafaunal extinction in causing ecological state shifts in North and South America. *Proc Natl Acad Sci USA* 113:856–861.
123. Daniau A-L, et al. (2013) Orbital-scale climate forcing of grassland burning in southern Africa. *Proc Natl Acad Sci USA* 110:5069–5073.
124. Zhou B, et al. (2007) Elemental carbon record of paleofire history on the Chinese Loess Plateau during the last 420 ka and its response to environmental and climate changes. *Palaeogeogr Palaeoclimatol Palaeoecol* 252:617–625.
125. van der Werf GR, et al. (2006) Interannual variability in global biomass burning emissions from 1997 to 2004. *Atmos Chem Phys* 6:3423–3441.
126. Caldararo N (2002) Human ecological intervention and the role of forest fires in human ecology. *Sci Total Environ* 292:141–165.
127. Lawson IT, Tzedakis PC, Roucoux KH, Galanidou N (2013) The anthropogenic influence on wildfire regimes: Charcoal records from the Holocene and Last Interglacial at Ioannina, Greece. *J Biogeogr* 40:2324–2334.
128. Smith FA, et al. (2016) Exploring the influence of ancient and historic megaherbivore extirpations on the global methane budget. *Proc Natl Acad Sci USA* 113:874–879.
129. Buizert C, Sowers T, Blunier T (2013) Assessment of diffusive isotopic fractionation in polar firn, and application to ice core trace gas records. *Earth Planet Sci Lett* 361: 110–119.
130. Bock J, Martinerie P, Witrant E, Chappellaz J (2012) Atmospheric impacts and ice core imprints of a methane pulse from clathrates. *Earth Planet Sci Lett* 349:98–108.
131. Bock M, et al. (2010) A gas chromatography/pyrolysis/isotope ratio mass spectrometry system for high-precision deltaD measurements of atmospheric methane extracted from ice cores. *Rapid Commun Mass Spectrom* 24:621–633.
132. Chappellaz J, et al. (1997) Changes in the atmospheric CH_4 gradient between Greenland and Antarctica during the Holocene. *J Geophys Res* 102:15987–15997.
133. Berger A, Loutre MF (1991) Insolation values for the climate of the last 10 million years. *Quat Sci Rev* 10:297–317.
134. Petit JR, et al. (1999) Climate and atmospheric history of the past 420,000 years from the Vostok ice core, Antarctica. *Nature* 399:429–436.
135. Dreyfus GB, et al. (2007) Anomalous flow below 2700 m in the EPICA Dome C ice core detected using delta O-18 of atmospheric oxygen measurements. *Clim Past* 3: 341–353.
136. Dreyfus G (2008) Dating an 800,000 year Antarctic ice core record using the isotopic composition of trapped air. PhD thesis (Princeton Univ, Princeton).
137. Bazin L, et al. (2013) An optimized multi-proxy, multi-site Antarctic ice and gas orbital chronology (AICC2012): 120-800 ka. *Clim Past* 9:1715–1731.
138. Bazin L, et al. (2016) Phase relationships between orbital forcing and the composition of air trapped in Antarctic ice cores. *Clim Past* 12:729–748.
139. Veres D, et al. (2013) The Antarctic ice core chronology (AICC2012): An optimized multi-parameter and multi-site dating approach for the last 120 thousand years. *Clim Past* 9:1733–1748.
140. Schwander J, Stauffer B, Sigg A (1988) Air mixing in firn and the age of the air at pore close-off. *Annals of Glaciology* 10:141–145.
141. Schwander J (1996) Gas diffusion in firn. *Chemical Exchange Between the Atmosphere and Polar Snow*, eds Wolff EW, Bales RC (Springer, Berlin), pp 527–540.
142. Sowers T, Bender M, Raynaud D, Korotkevich YS (1992) $\delta^{15}N$ of N_2 in air trapped in polar ice: A tracer of gas transport in the firn and a possible constraint on ice age-gas age differences. *J Geophys Res* 97:15,683–15,697.
143. Dreyfus GB, et al. (2010) Firn processes and $\delta^{15}N$: Potential for a gas-phase climate proxy. *Quat Sci Rev* 29:28–42.
144. Eggleston S, Schmitt J, Bereiter B, Schneider R, Fischer H (2016) Evolution of the stable carbon isotope composition of atmospheric CO_2 over the last glacial cycle. *Paleoceanography* 31:434–452.
145. Bender ML (2002) Orbital tuning chronology for Vostok climate record supported by trapped gas composition. *Earth Planet Sci Lett* 204:275–289.
146. Landais A, et al. (2006) Firn-air $\delta^{15}N$ in modern polar sites and glacial-interglacial ice: A model-data mismatch during glacial periods in Antarctica? *Quat Sci Rev* 25:49–62.
147. Enting IG (1987) On the use of smoothing splines to filter CO_2 data. *J Geophys Res Atmos* 92:10977–10984.
148. Frezzotti M, et al. (2004) Geophysical survey at Talos Dome, East Antarctica: The search for a new deep-drilling site. *Annals of Glaciology* 39:423–432.
149. Iaccarino A (2017) Taldice drill site information summary (Taldice Project). Available at www.taldice.org/project/summary/index.php. Accessed March, 14, 2017.
150. AARI (2017) Surface wind and air pressure field. Station Vostok. Available at www.aari.aq/stations/vostok/vostok_en.html#wind. Accessed March, 14, 2017.
151. Whiticar M, Schaefer H (2007) Constraining past global tropospheric methane budgets with carbon and hydrogen isotope ratios in ice. *Philos Trans A Math Phys Eng Sci* 365:1793–1828.
152. Walter KM, Zimov SA, Chanton JP, Verbyla D, Chapin FS, 3rd (2006) Methane bubbling from Siberian thaw lakes as a positive feedback to climate warming. *Nature* 443:71–75.
153. Levine JG, et al. (2011) Reconciling the changes in atmospheric methane sources and sinks between the Last Glacial Maximum and the pre-industrial era. *Geophys Res Lett* 38:L23804.
154. Whiticar MJ (1993) Stable Isotopes and Global Budgets. *Atmospheric Methane: Sources, Sinks, and Role in Global Change*, ed Khalil MAK (Springer, Berlin), pp 138–167.
155. Feilberg KL, Griffith DWT, Johnson MS, Nielsen CJ (2005) The ^{13}C and D kinetic isotope effects in the reaction of CH_4 with Cl. *Int J Chem Kinet* 37:110–118.
156. Levine JG, Wolff EW, Jones AE, Sime LC (2011) The role of atomic chlorine in glacial-interglacial changes in the carbon-13 content of atmospheric methane. *Geophys Res Lett* 38:L04801.
157. Friedl MA, et al. (2010) *MODIS Collection 5 Global Land Cover: Algorithm Refinements and Characterization of New Datasets, 2001-2012, Collection 5.1 IGBP Land Cover* (Boston Univ, Boston).
158. Channan S, Collins K, Emanuel WR (2014) *Global Mosaics of the Standard MODIS Land Cover Type Data* (Univ of Maryland and the Pacific Northwest National Laboratory, College Park, MD).
159. Kessler JD, et al. (2011) A persistent oxygen anomaly reveals the fate of spilled methane in the deep Gulf of Mexico. *Science* 331:312–315.

Supporting Information

Bock et al. 10.1073/pnas.1613883114

SI Text

Corrections of Isotope Data to Address Fractionation in the Firn Caused by Diffusion. Air in firn is subject to diffusion (140). Accordingly, we applied corrections to our measured ice core isotope data as explained in the following two sections.

Correction of $\delta^{13}CH_4$ and $\delta D(CH_4)$ data because of gravitational settling in the firn. Gravitational settling creates a gradient with heavier isotopologues accumulating at the bottom of the diffusive zone. For the heavier isotopes, an enrichment in the range of 0.2–0.5‰ per mass difference is observed in air bubbles of an ice core and can be corrected for using $\delta^{15}N_2$ measurements (141, 142). Because only the mass difference is decisive, this approach holds for both $\delta^{13}CH_4$ and $\delta D(CH_4)$. For $\delta^{13}CH_4$, we used interpolated $\delta^{15}N_2$ records from EDC (51, 136, 143), TALDICE (144), and Vostok (145). Concerning $\delta D(CH_4)$, we used the same procedure and datasets for EDC (51, 136, 143). However, for EDML, no complete dataset covering all our samples is available, and we used the mean value (0.44‰) of all EDML $\delta^{15}N_2$ values given in ref. 146. Note that the glacial/interglacial difference in the last mentioned dataset is only about 0.05‰, and hence, the error introduced because of this simplified approach is much smaller than other measurement uncertainties for $\delta D(CH_4)$. All $\delta^{13}CH_4$ and $\delta D(CH_4)$ data presented in the figures of this contribution have been corrected for gravitational settling in the firn.

Correction of $\delta^{13}CH_4$ data because of diffusive isotopic fractionation in the firn. Isotopologues of a trace gas species (e.g., $\delta^{13}CH_4$) have a different diffusion constant; hence, if a concentration gradient between the free atmosphere and the bottom of the firn is present, the isotopic signature of the original atmospheric signal changes while it is carried down to the lock-in depth. The phenomenon called diffusive fractionation is described in detail in ref. 129. The authors also provide the mathematical tools to quantify the effect. Using this approach allowed us to calculate the diffusive fractionation correction for our $\delta^{13}CH_4$ data.

The diffusive column height for each data point was calculated using interpolated $\delta^{15}N_2$ records from EDC (51, 136, 143), TALDICE (144), and Vostok (145). The CH_4 mixing ratio and its annual changing rate have been determined using a spline approximation [1,000-y cutoff frequency (147)] of the EDC CH_4 data (4). Other than the values given in ref. 129, we further used estimates for the mean annual site temperatures [EDC: −54 °C (129), TALDICE: −41 °C (148), and Vostok: −55 °C (134)] and the mean annual surface air pressure [EDC: 694 mbar (129), TALDICE: 721 mbar (149), and Vostok: 624 mbar (150)] to calculate the diffusion fractionation correction. All new $\delta^{13}CH_4$ data presented in the figures of this contribution have been corrected for diffusive isotopic fractionation in the firn. The effect for all of our samples is small, because we did not measure $\delta^{13}CH_4$ samples from time periods with rapidly changing CH_4 mixing ratio. The changes of the measured values are between −0.18‰ and +0.08‰, hence not relevant for any of our conclusions.

The effect is of the same size for $\delta D(CH_4)$. Because the uncertainties of this parameter are larger, we choose not to correct our $\delta D(CH_4)$ data for diffusive isotopic fractionation in the firn.

Definition of Time Slices for "Typical" Glacial and Interglacial Levels. We defined time slices that are intended to represent "typical levels" within our isotope records. These time slices are used to quantitatively describe glacial/interglacial amplitudes of $[CH_4]$, $\delta^{13}CH_4$, and $\delta D(CH_4)$ and assess the shift of both isotopes for the Holocene and the LGM compared with earlier interglacials and glacials, respectively. The time interval definition in Fig. S1 uses data for glacial maxima characterized by CO_2 concentrations below 210 ppm and CH_4 concentrations below 420 ppb (4, 110). Similarly, data used for interglacial periods have CO_2 concentrations above 260 ppm and CH_4 concentrations above 500 ppb (4, 110). The time periods used are illustrated in Fig. S1, where red and blue shading highlights data for interglacial and glacial time slices, respectively. In Table S1, we summarize $[CH_4]$, isotope mean and median values of the used time slices.

Note that the intention of this definition is only a simplified first-order view of the presented records, whereas our data show variations within the chosen time slices rather than stable levels. Note that the time interval with the most ^{13}C-depleted values between 115 and 120 ka BP is not included in the MIS 5.5 typical level, because $[CH_4]$ is already below typical interglacial levels. This $\delta^{13}CH_4$ minimum is discussed as a special feature in the text.

Box Model to Constrain the CH_4 Budget. Natural methane sources can be differentiated according to their isotopic signatures. For instance, BB and GEM emit relatively isotopically heavy methane (i.e., enriched in ^{13}C and deuterium compared with the averaged source mix). However, the largest natural source type—microbial emissions largely from wetlands—emits methane with an isotopic fingerprint slightly lower in $\delta^{13}CH_4$ and $\delta D(CH_4)$ than the source mix. In addition, isotopic fractionation by the sinks leads to heavier methane in the atmosphere compared with the emissions.

Box model: Setup. To constrain the (isotopic) CH_4 budget, we used the box model presented in refs. 32 and 36, which consists of four boxes (northern and southern troposphere and stratosphere) with prescribed air mass exchange. This model allows one to assess maximal GEM and increased emissions by BB for the Holocene and the LGM compared with previous interglacials and glacials, respectively. To this end, CH_4 sources (both emission strengths and isotopic source signatures) (Table S2) and relative sink contribution (Table S3) are varied within prescribed ranges in the model (refs. 13, 22, 32, 36, and 63 and references therein). The model is run into steady state, and the equilibrium value of the southern tropospheric box is compared with our data constraints (Table S1) for each of the time slices. If the modeled $[CH_4]$, $\delta^{13}CH_4$, and $\delta D(CH_4)$ values are compatible within the uncertainty (Table S1) with the data constraint, the emission values are recorded as a possible CH_4 budget solution. For each time slice, 10,000 valid runs have been collected.

Box model: Sources. To be consistent with recent work on the current methane budget (63), we distinguish only three source categories here: GEM, BB, and a microbial source including natural sources, such as wetlands, termites, and naturally occurring ruminants. Isotopic signatures of the sources are based on previous work (refs. 13, 32, and 36 and references therein) and the collection in ref. 63 with some modifications. Table S2 shows the $\delta^{13}CH_4$ values used for the microbial source, BB, and GEM according to ref. 63 with some modifications (see below) and $\delta D(CH_4)$ values (refs. 13 and 22 and references therein).

For the interglacial $\delta^{13}CH_4$ source signatures of the microbial source, BB emission, and GEM, we used the global value given in ref. 63 with two modifications for the microbial source. (*i*) The modern microbial source used in ref. 63 includes anthropogenic emissions from ruminants and landfills, which bias the natural isotopic source signature. As we investigated the natural budget in this contribution, we removed the waste CH_4 source (which leads to a heavier source mix signature) and decreased emissions

from ruminants, which at present largely reflect livestock in ref. 63, by 80 ± 20% (which leads to a lighter source mix signature). In the end, these adjustments essentially canceled each other and led to a global mean microbial source signature that is the same as the recent value given in ref. 63 within the error limits. Accordingly, we used a global mean microbial source signature of −62.2 ± 1.0‰ in our model. (*ii*) The value given in ref. 63 represents a global average; however, previous work (refs. 32, 35–37, 75, 151, and 152 and references therein) has shown that high-latitude wetland sources are depleted in ^{13}C and deuterium. Because the high-latitude wetland sources are mainly located in the Northern Hemisphere, a difference in the isotopic source signatures of the two hemispheres is observed. To account for this difference, we used the geographically resolved wetland emission estimate in ref. 10 and the published data on the IPD of the methane mixing ratio (9, 79, 89, 132) to assess how much of the total wetland emissions are located in the Northern Hemisphere. Aggregating the distribution in ref. 10 into three categories (tropical south, tropical north, and boreal north) leads to a northern fraction of wetland source emissions of 0.6. However, our model runs are consistent with the IPD constraint (9, 79, 89, 132) only when using a northern fraction of 0.7 for the microbial source. This higher ratio is achieved by shifting 17 Tg CH_4 a^{-1} from the southern tropical to the northern tropical region compared with ref. 10. We stress that this small difference is not in conflict with the estimate in ref. 10, which assessed the present day emissions dominated by the anthropogenic sources. In a next step, we assigned $\delta^{13}CH_4$ and $\delta D(CH_4)$ source signatures for the boreal (high-latitude) source, which are 6 and 50‰ lower, respectively, than the low-latitude sources (refs. 32, 35–37, 75, 151, and 152 and references therein). Using the global source signature value in ref. 63 (see above), this adjustment led to a Northern Hemisphere microbial source signature of −62.6‰ and a Southern Hemisphere microbial source signature of −61.4‰ in $\delta^{13}CH_4$. For $\delta D(CH_4)$, we use −323‰ for the Northern Hemisphere and −313‰ for the Southern Hemisphere for the microbial source signature in our model (Table S2). These numbers lead to global source signatures of our microbial source of −62.2 and −320‰ for $\delta^{13}CH_4$ and $\delta D(CH_4)$ as proposed in refs. 63 and 13, respectively.

As shown in refs. 25 and 34, isotopic signatures of biogenic sources (microbial and BB) may have changed on glacial/interglacial timescales. According to ref. 25, we estimate that about one-half of the glacial/interglacial amplitude of $\delta^{13}CH_4$ is caused by environmental changes leading to source signature changes, whereas the other one-half is accounted for by source mix changes. Hence, we attributed one-half of the averaged $\delta^{13}CH_4$ differences of MIS 12 minus MIS 11 and MIS 6 minus MIS 5 (Table S1) to a $\delta^{13}CH_4$ shift of our microbial and BB source signatures and used these shifted source signatures in our model for glacial time slices. Accordingly, the microbial and the BB $\delta^{13}C$ source signature ranges for glacial time slices are heavier (higher $\delta^{13}CH_4$) in our model by 2.6‰ compared with interglacial runs (Table S2).

The geographic distribution of the emissions (i.e., the fraction that is emitted into the northern model troposphere compared with the Southern Hemisphere) has been adjusted, such that the modeled IPD of $[CH_4]$ is in line with data constraints for the Holocene and the LGM (9, 79, 89, 132). Our best estimates for both interglacial and glacial model setups are northern emissions fractions of 0.7 for the microbial source, 0.7 for BB, and 0.6 for GEM. Note that no IPD information is available for the oldest four time slices used in this study, because no or no reliable atmospheric CH_4 values are available for the Northern Hemisphere from Greenland ice cores. Hence, we used the same source distribution for older time slices (identical input parameters for the older interglacials, MIS 5.5 and MIS 11.3, as for the Holocene and identical input parameters for the older glacials, MIS 6 and MIS 12, as for the LGM).

To exclude an overestimation of the emissions into the Northern Hemisphere, we additionally performed sensitivity runs where we assumed no latitudinal difference in the CH_4 emissions (i.e., northern emission fractions of 0.5 for all three source categories). Because an IPD is evident at present and persistent for the last 25,000 y (9, 79, 89, 132), this exercise is considered a minimum conservative endmember for the true hemispheric source distribution. Accordingly, we expect true BB/GEM to be between the results of our best guess model runs and these sensitivity runs. For the sensitivity runs, identical emission values (Table S2) and targets (Table S1) have been used with one exception. The calculation of isotopic source signatures according to the procedure described above yielded slightly higher numbers for the microbial source for both $\delta^{13}CH_4$ and $\delta D(CH_4)$, because 15 Tg CH_4 a^{-1} had to be shifted from the northern tropical to the southern tropical region compared with the distribution given in ref. 10. The changed isotopic signatures of the microbial source for the sensitivity model runs are given in Table S2.

Krypton measurement artifacts and consequences for the CH_4 budget. We stress that our new ice core $\delta^{13}CH_4$ and $\delta D(CH_4)$ measurements presented in this study are free of the krypton (Kr) measurement artifact described in refs. 46–48, which arises if Kr interferences are not excluded during the mass spectrometric (MS) analyses. Previous studies relied on measurements including a Kr effect, which leads to biased $\delta^{13}CH_4$ values that are higher. Specifically, we note that the assessment in ref. 63 is based on Greenland ice core data for the Late Holocene in ref. 64, which were not corrected for a Kr interference during the measurement. Using the differences of Sapart's (64) $\delta^{13}CH_4$ values with and without Kr effect for standard air bottles with different $[CH_4]$/Kr ratios given in table 2 of ref. 48, we can roughly assess the bias of the Late Holocene $\delta^{13}CH_4$ dataset. For this exercise, we assume a mixing ratio around 700 ppb (64). Furthermore, assuming no additional amount dependence of $\delta^{13}CH_4$ in this dataset (which could amplify or dampen the observation), we calculate an offset of these data of approximately +1.15‰. If true, the Late Holocene atmospheric value was lower by this amount. As a consequence, lower $\delta^{13}CH_4$ constraints lead to lower BB and/or GEM estimates compared with the assessment in ref. 63. Using our observed differences of older time periods (Table S1) to scale emissions based on Fig. 2 leads to a reduction of GEM by roughly 6 Tg CH_4 a^{-1} compared with the value given in ref. 63. Note that the total GEM estimate is also strongly dependent on the assumed BB emissions as discussed in the text.

Box model: Sinks. The atmospheric lifetime of methane has been kept constant at 8 y for all performed runs. This approach is in line with several atmospheric chemistry modeling studies, which show little change in the overall lifetime of methane for different climate periods (40–42, 153). In our revised box model, four sinks are implemented (OH oxidation in the troposphere, methanotrophy in soils, a stratospheric sink, and a Cl sink in the marine boundary layer) with fixed fractionation factors (Table S3) (13, 154–156). Note that these sinks differ greatly in their fractionation factors. Accordingly, although the overall lifetime may have stayed constant over time, a change in the relative fraction of each sink to the total lifetime may have had an impact on the isotopic composition of the atmosphere. Moreover, the effect of such sink contribution effects would have a different impact on $\delta^{13}CH_4$ and $\delta D(CH_4)$. Atmospheric methane removal through the four sink processes in our model is scaled according to ref. 10; however, in our Monte Carlo approach, we allow the relative contributions of each sink to vary within certain limits to account for uncertainties in our understanding of the sink attributions (10). Accordingly, the fractional sink of each sink process (in Tg CH_4 a^{-1}) was varied independently by ±15%. The sum of all individual sink contributions in each Monte Carlo run was then

scaled to balance the total emission for the lifetime of 8 y required to obtain the targeted CH_4 mixing ratio. The resulting ranges of the relative contribution of each sink are given in Table S3.

Also, the sink contributions are different in both hemispheres. The hemispheric distribution of the model sinks is constant for all runs and summarized in Table S3. The tropospheric and stratospheric sinks are split half and half between the northern and southern boxes. The soil sink and the marine chlorine sink are distributed according to the difference in land and ocean coverage in both hemispheres. We choose a partitioning according to the Global Land Cover Facility with unevenly distributed northern fractions of 0.74 and 0.43 for the soil and marine chlorine sinks, respectively (Table S3) (157, 158).

Box model: Results. Contrary to our previous work (32, 36), we do not present normalized probability density functions (nPDFs) for the box model results. This change is because of the fact that using nPDFs is misleading and suggests a likelihood for emission strengths of different sources, which in fact, is an artifact of the Monte Carlo process. Without additional knowledge, each accepted box model solution in line within the uncertainties with the (isotopic) data constraint is equally likely. For example, the higher numbers of accepted model solutions in ref. 32 for short lifetimes in the glacial do not imply that a shorter lifetime is more realistic. Instead, they reflect only that, in the box model approach, where all parameters are varied independently, it is much easier to achieve low glacial CH_4 concentrations by reducing only one parameter, the lifetime, instead of reducing the emissions of all source types at the same time by the correct amount, while not violating the (isotopic) CH_4 budget. The only valid information that should be drawn from the model results is the field of possible emission strengths for each of the given sources. Accordingly, we can exclude all scenarios that do not fulfill the ice core constraint. In this study, we avoid these pitfalls of nPDFs but go beyond previous Monte Carlo approaches by analyzing the accepted model runs to find functional relationships between the emissions of different source types (Fig. 2 and Fig. S7). For example, Fig. 2 shows the variation of possible GEMs under given BB emissions. Similarly, one can derive information for the microbial source for given numbers of BB and/or GEM as shown in Fig. S7 *A* and *B*. For instance, selecting 25 Tg CH_4 a^{-1} for BB and 30 Tg CH_4 a^{-1} for GEM during interglacials, the microbial source strength is roughly between 150 and 230 Tg CH_4 a^{-1}.

The uncertainty of the isotopic signature of the sources and the fractions of the sinks is intrinsically implemented in the model results, because we allowed the Monte Carlo process to pick values from broad ranges of isotopic source signatures (Fig. S7 *C* and *D* and Table S2) and the sink fractions (Table S3). Fig. S7 *C* and *D* shows that the model favors lower emissions from the microbial source for the Holocene and the LGM compared with older time slices, because the heavier isotope targets are more easily achieved by higher emissions of BB and/or GEM.

Results for the sensitivity analysis on the hemispheric distribution of sources are presented in Fig. S7 *E* and *F*. It is not straightforward to reliably quantify the IPD in the past, but it is clear that, for a minimum (zero) IPD in [CH_4], our BB and GEM maximum estimates are not significantly higher compared with the standard model runs.

Note that, for emissions from marine clathrates (and generally, submarine GEM), which are part of our GEM model source, our scenarios do not take into account isotopic fractionation during oxidation in the water column. This process leads to heavier (higher) numbers in both isotopes for methane reaching the air/sea interface (27, 29, 31, 36, 39, 54, 159). Assuming heavier fingerprints for clathrate emissions into the atmosphere reduces their share to the global budget. The same is true if a heavier carbon isotopic signature is assumed for some sources of GEM as listed in table 1 of ref. 29.

Supplementary Graphs. An overview of all data presented in this study is shown in Fig. S1, which highlights the time intervals used to determine the targets for the box model runs. We underline that Fig. S1 presents additional Bern $\delta^{13}CH_4$ data between 25 and 80 ka BP, which are not presented in Fig. 1 and have been partly shown in our technical article on the measurement system (47). Furthermore, we present the data shown in Fig. 1 in enhanced and zoomed versions. First, the interglacial periods are highlighted (Fig. S2) and set into context with a recently published speleothem monsoon proxy record (70). Second, we zoom into three presented time intervals: LGM/Holocene, MIS 6/MIS 5.5, and MIS 12/MIS 11.3 (Figs. S3–S5). Finally, we present a figure comparing previously published data to our records (Fig. S6).

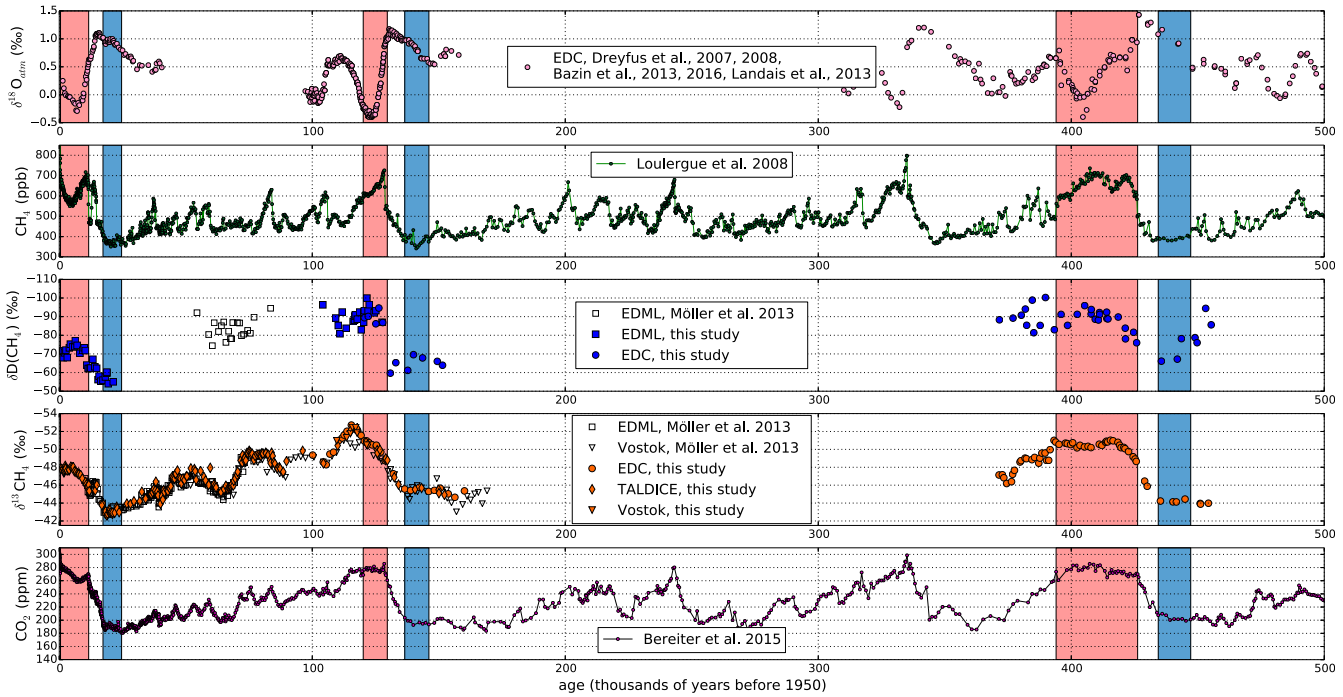

Fig. S1. Ice core records of $\delta^{18}O_{atm}$ (51, 135–138), [CH_4] (4), its stable isotopes [this study and data measured in refs. 25 and 32; note that the dataset by Fischer et al. (32) was corrected for a Kr effect as presented in ref. 25], and [CO_2] (110). The red and blue shading indicates interglacial and glacial time slices, respectively, used to calculate numbers for Table S1. This plot also shows additional Bern $\delta^{13}CH_4$ data between 25 and 80 ka BP, which are not presented in Fig. 1.

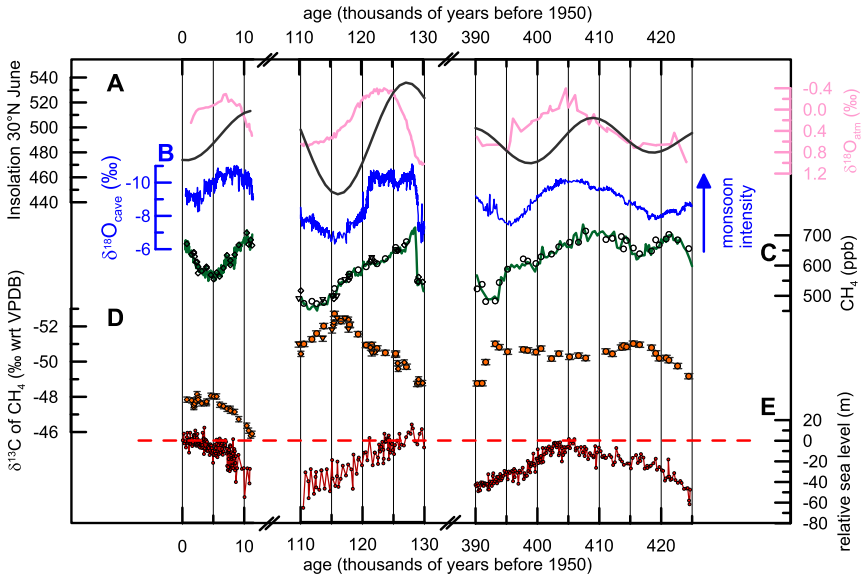

Fig. S2. Highlighted data for the investigated interglacial periods (note the breaks in the *x* axis). (*A*) Solar insolation in June at 30° N (133) and atmospheric $\delta^{18}O$ from EDC (51, 135–138); (*B*) speleothem $\delta^{18}O$ data from Sanbao cave (70); (*C*) [CH_4] (4) (green line) and data from this study (open diamonds are from TALDICE, open circles are from EDC, and open triangles are from Vostok samples); (*D*) $\delta^{13}CH_4$ from TALDICE, EDC, and Vostok [5G; this study; symbols are chosen as for [CH_4]; the error bars represent the 1-sigma SD of ice core replicates (47): 0.15‰]; and (*E*) relative sea level as reconstructed from marine sediment records from the Red Sea (108). Ice core records are given on the Antarctic ice core chronology (AICC2012) gas age scale (137, 139), and insolation, speleothem data, and sea level are given on their individual age scales. Note the inverse direction of all isotope axes.

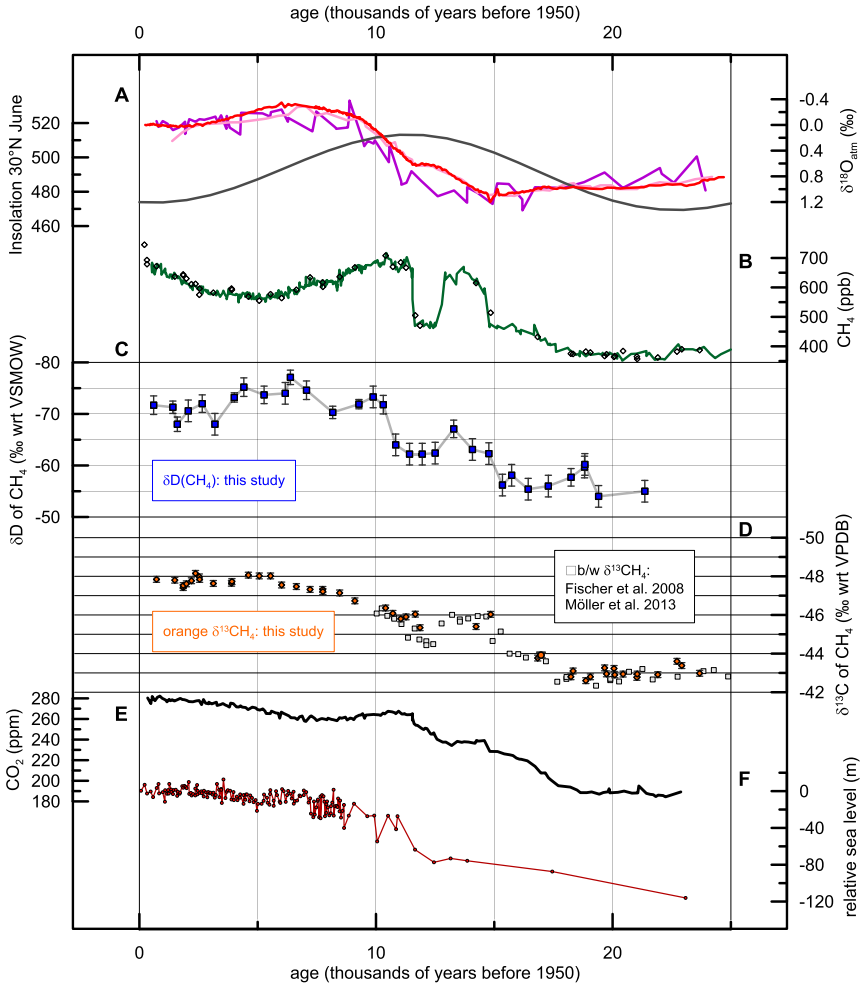

Fig. S3. Paleoclimatic records of Fig. 1 zoomed for the LGM and the Holocene. From top to bottom, the panels show (*A*) solar insolation in June at 30° N (133) and atmospheric $\delta^{18}O$ from Vostok (purple) (134), EDC (light pink) (51, 135–138), and Siple Dome (red) (84); (*B*) [CH4] (ref. 4 and data from this study); (*C*) $\delta D(CH_4)$ from EDML and EDC (this study; error bars are 1-sigma SDs of reference air measurements); (*D*) $\delta^{13}CH_4$ from Talos Dome, EDC, and Vostok (5G; this study; the error bars represent the 1-sigma SD of ice core replicates (47): 0.15‰) and data from EDML and Vostok (25, 32); (*E*) [CO_2] (110); and (*F*) relative sea level as reconstructed from Red Sea sediment cores (108).

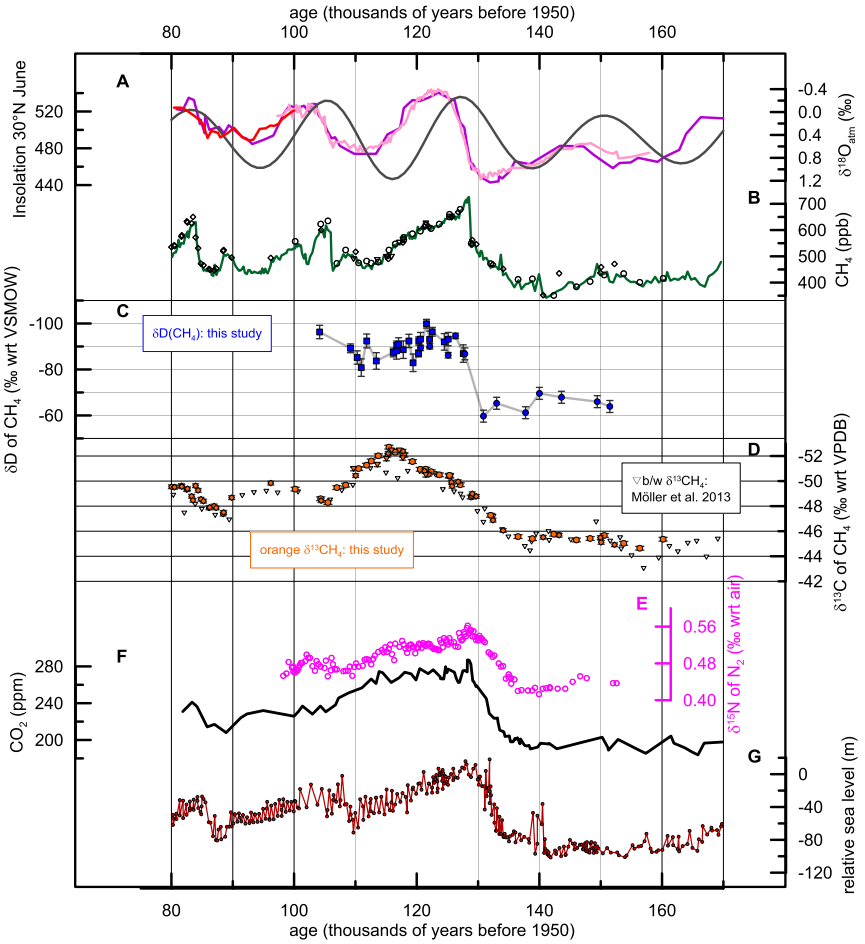

Fig. S4. Paleoclimatic records of Fig. 1 zoomed for MIS 6 and MIS 5.5. From top to bottom, the panels show (*A*) solar insolation in June at 30° N (133) and atmospheric $\delta^{18}O$ from Vostok (purple) (134), EDC (light pink) (51, 135–138), and Siple Dome (red) (84); (*B*) [CH_4] (ref. 4 and data from this study); (*C*) $\delta D(CH_4)$ from EDML and EDC (this study; error bars are 1-sigma SDs of reference air measurements); (*D*) $\delta^{13}CH_4$ from Talos Dome, EDC, and Vostok (5G; this study; the error bars represent the 1-sigma SD of ice core replicates (47): 0.15‰) and data from EDML and Vostok (25, 32). The graph is extended by *E* showing $\delta^{15}N$ of air (51). Panel (*F*) shows [CO_2] (110); and (*G*) relative sea level as reconstructed from Red Sea sediment cores (108).

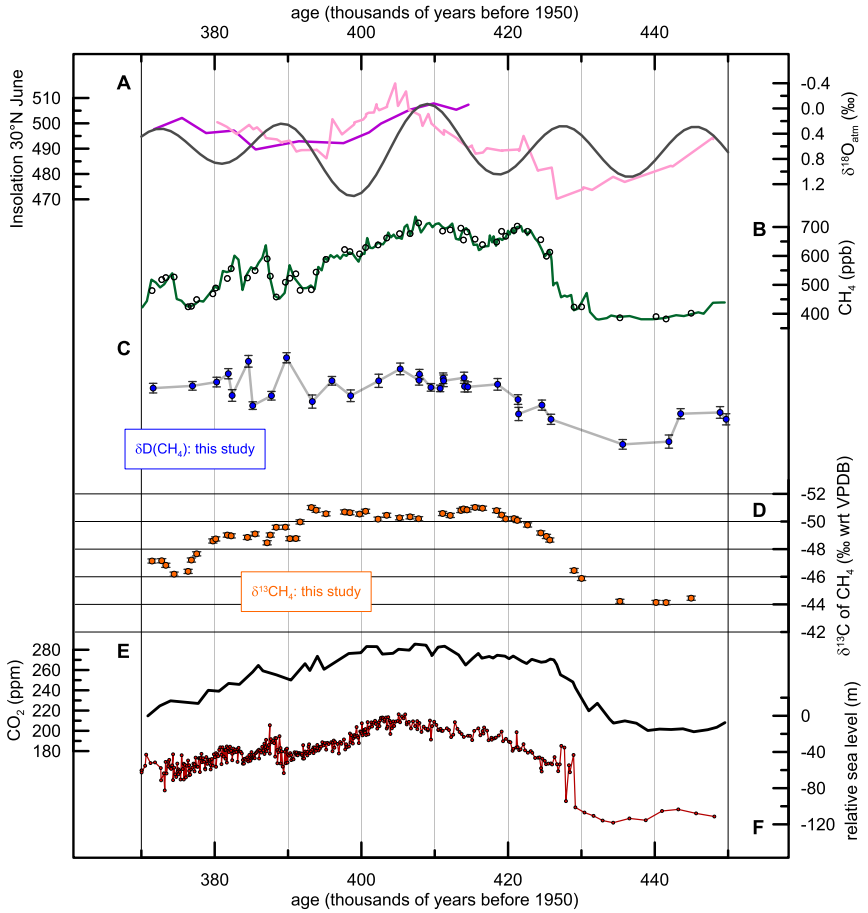

Fig. S5. Paleoclimatic records of Fig. 1 zoomed for MIS 12 and MIS 11.3. From top to bottom, the panels show (*A*) solar insolation in June at 30° N (133) and atmospheric $\delta^{18}O$ from Vostok (purple) (134), and EDC (light pink) (51, 135); (*B*) [CH_4] (ref. 4 and data from this study); (*C*) $\delta D(CH_4)$ from EDML and EDC (this study; error bars are 1-sigma SDs of reference air measurements); (*D*) $\delta^{13}CH_4$ from Talos Dome, EDC, and Vostok (5G; this study; the error bars represent the 1-sigma SD of ice core replicates (47): 0.15‰) and data from EDML and Vostok (25, 32); (*E*) [CO_2] (110); and (*F*) relative sea level as reconstructed from Red Sea sediment cores (108).

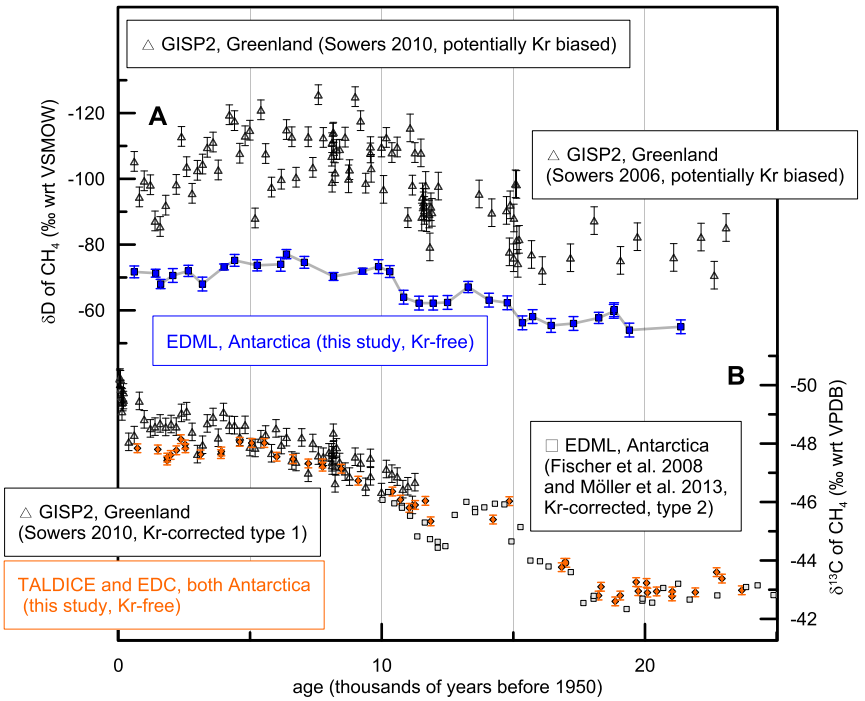

Fig. S6. Comparison of previously published datasets with this study for the last 25,000 y. (*A*) $\delta D(CH_4)$ by Sowers (31, 49) from the Greenland core Greenland Ice Sheet Project (GISP2) and data from this study from EDML (Antarctica). Note that the offset of the two datasets is caused by a not well-quantified IPD in $\delta D(CH_4)$ (approximately −16‰) plus an interlaboratory-scale offset (46). Additional slight differences might occur, because the datasets by Sowers (31, 49) are not free from a Kr effect, whereas $\delta D(CH_4)$ data from this study are measured without any Kr interference (46). (*B*) $\delta^{13}CH_4$ from the Greenland core GISP2 (49), data from EDML (32), and data from this study from TALDICE and EDC (all three cores from Antarctica). Also for $\delta^{13}CH_4$, the IPD is not well-known (approximately −0.5‰). We stress that only the $\delta^{13}CH_4$ data of this study are measured without any Kr interference (47, 48). The data by Sowers et al. (49) and Fischer et al. (32) have been corrected for a Kr effect by ref. 25 using two different approaches: the correction ($\Delta\delta^{13}C_{Kr}$) of Vostok and GISP2 data measured at the Pennsylvania State University were inferred indirectly from CH_4 mixing ratios (referred to as type 1), whereas for the EDML record, the correction was based on the Kr-induced anomaly derived from the ion current ratios (type 2; section 1.3 of ref. 25 has a detailed description of both approaches).

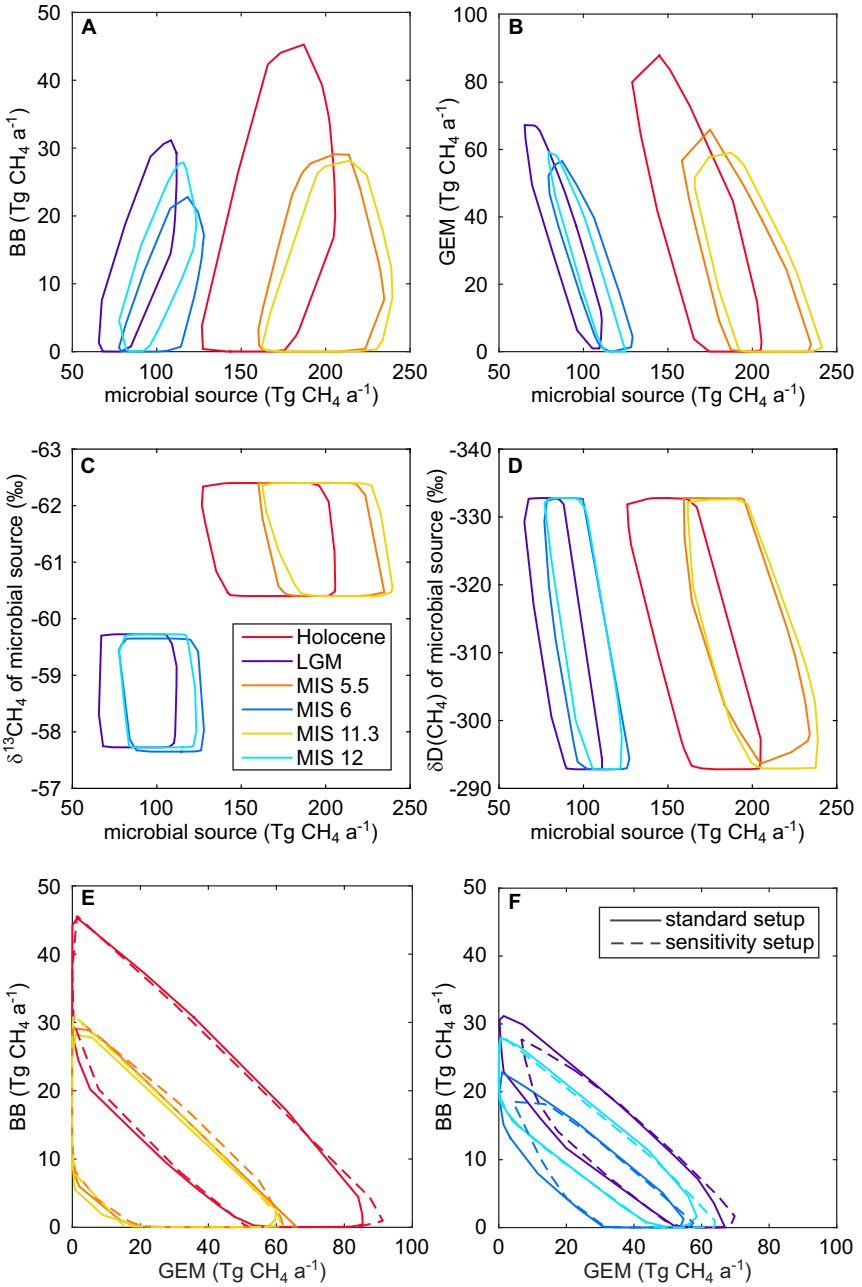

Fig. S7. Box model results fulfilling the ice core constraints. Each line encloses 10,000 valid realizations of the Monte Carlo model covering the parameter spaces of six time periods (Table S1). The Matlab function convhull() was used to determine the envelope around the solutions for each time slice. Legends are valid for all subpanels. (*A* and *B*) Shown are emission strengths of the microbial model source in relation to (*A*) BB and (*B*) GEM for interglacial and glacial times. (*C* and *D*) Shown are emission strengths of the microbial model source in relation to its isotopic signature: (*C*) $\delta^{13}CH_4$ and (*D*) $\delta D(CH_4)$ for interglacial and glacial times. $\delta^{13}CH_4$ of the microbial source is chosen to be heavier by 2.6‰ for glacials (in the text and Table S2). (*E* and *F*) Box model results of the standard setup (lines) and the sensitivity runs with zero IPD of $[CH_4]$ (dashed lines). Shown are emission strengths of BB in relation to GEM. *E* shows results for interglacials, and *F* shows results for glacials.

Table S1. Quantitative estimates of the mean methane stable isotopic signature (this study) and mixing ratios (4) characterizing the time slices used in the box model

Minimum gas age AICC (ka BP)	Maximum gas age AICC (ka BP)	Used ice core(s)	*N*	Mean	SD	Median	Minimum	Maximum	Corresponding MIS
				$\delta^{13}CH_4$ (‰ wrt VPDB)					
0.5	11.6	TALDICE and EDC	26	−47.4	0.7	−47.6	−48.2	−45.8	MIS 1
17.3	24.6	TALDICE	15	−43.0	0.3	−42.9	−43.6	−42.6	MIS 2
120.1	129.7	TALDICE, EDC, Vostok	16	−50.1	0.7	−50.4	−51.0	−48.7	MIS 5.5
136.6	146.1	TALDICE and EDC	5	−45.5	0.2	−45.5	−45.8	−45.3	MIS 6
394.0	426.6	EDC	26	−50.3	0.6	−50.5	−51.0	−48.7	MIS 11.3
434.0	447.2	EDC	4	−44.2	0.1	−44.2	−44.4	−44.1	MIS 12
				$\delta D(CH_4)$ (‰ wrt VSMOW)					
0.5	11.6	EDML	18	−71	4	−72	−77	−62	MIS 1
17.3	24.6	EDML	5	−57	3	−58	−60	−54	MIS 2
120.1	129.7	EDML and EDC	14	−92	4	−92	−100	−86	MIS 5.5
136.6	146.1	EDC	3	−66	4	−68	−70	−61	MIS 6
394.0	426.6	EDC	18	−88	5	−89	−96	−76	MIS 11.3
434.0	447.2	EDC	3	−71	7	−67	−78	−66	MIS 12
				$[CH_4]$ (ppb)					
0.5	11.6	EDC	280	618	40	612	549	717	MIS 1
17.3	24.6	EDC	44	377	15	375	351	409	MIS 2
120.1	129.7	EDC	47	634	45	627	535	726	MIS 5.5
136.6	146.1	EDC	17	382	24	375	342	432	MIS 6
394.0	426.6	EDC	87	649	47	658	498	736	MIS 11.3
434.0	447.2	EDC	9	391	8	392	381	405	MIS 12

Note the large SDs, especially for $\delta^{13}CH_4$ and $[CH_4]$ during interglacials, indicative of the large signal ranges observed within these time periods (compare Fig. 1 and Figs. S2–S5). Red and blue colors represent interglacial and glacial time slices, respectively, in line with colored bars in Fig. S1. Columns from left to right give the minimal and maximal gas ages of the analyzed time periods on the Antarctic ice core chronology (AICC 2012) age scale; the names of the ice cores used; the number of samples (*N*), average (mean), SD, median, minimum value, and maximum value for $[CH_4]$, $\delta^{13}CH_4$, $\delta D(CH_4)$; and the MIS roughly corresponding to the ice core time slices.

Table S2. Ranges of isotopic source signatures and source strengths used as model input

Source category	$\delta^{13}C$-CH_4 minimum (‰ wrt VPDB)	$\delta^{13}C$-CH_4 maximum (‰ wrt VPDB)	δD-CH_4 minimum (‰ wrt VSMOW)	δD-CH_4 maximum (‰ wrt VSMOW)	Global source strength minimum (Tg CH_4 a^{-1})	Global source strength maximum (Tg CH_4 a^{-1})
Standard model setup						
Interglacials						
Microbial source (south)	−62.4	−60.4	−332.8	−292.8	50	250
Microbial source (north)	−63.6	−61.6	−343.1	−303.1		
BB	−24.7	−20.0	−255.0	−195.0	0	60
GEM	−44.9	−43.2	−205.0	−165.0	0	120
Glacials						
Microbial source (south)	−59.7	−57.7	−332.8	−292.8	20	150
Microbial source (north)	−60.9	−58.9	−343.1	−303.1		
BB	−22.0	−17.3	−255.0	−195.0	0	60
GEM	−44.9	−43.2	−205.0	−165.0	0	120
Adjusted microbial source for sensitivity runs (assuming no IPD of $[CH_4]$)						
Interglacials						
Microbial source (south)	−62.3	−60.3	−332.8	−292.8	50	250
Microbial source (north)	−64.0	−62.0	−347.3	−307.3		
Glacials						
Microbial source (south)	−59.6	−57.6	−332.8	−292.8	20	150
Microbial source (north)	−61.3	−59.3	−347.3	−307.3		

For every Monte Carlo model run, values for $\delta^{13}CH_4$, $\delta D(CH_4)$, and the source strengths of each of three model source categories have been randomly picked from the given intervals. wrt, with respect to. The Matlab function unifrnd() has been used to generate continuous uniform random numbers. References and adjustments for the given isotopic signatures are described in detail in *SI Text* (refs. 13, 22, 32, 36, and 63 and references therein). Note that, concerning the microbial source, different isotopic signatures for the Southern Hemisphere and Northern Hemisphere are used. All source strengths are given as global values and distributed between the hemispheres according to information given in the text. Note the changed isotopic signatures for the microbial source for the sensitivity runs that assume no IPD of CH_4.

Table S3. Model sink fractions, isotopic fractionation factors, and hemispheric distribution

Sink	Sink fraction minimum (%)	Sink fraction maximum (%)	Fractionation factor ε for $\delta^{13}CH_4$ (‰)	Fractionation factor ε for $\delta D(CH_4)$ (‰)	Northern Hemisphere fraction of sink (%)
Tropospheric OH	78.8	84.8	−5.4	−231	50
Stratospheric loss	7.6	11.0	−22	−80	50
Soils	3.9	5.6	−12	−160	73.8
Tropospheric Cl	3.4	5.0	−60	−470	43.1

For every Monte Carlo model run, sink fractions of the individual sink processes have been randomly picked from the given intervals to account for uncertainties in the sink apportionment. Fractionation factors and hemispheric distribution have been kept constant for all model runs.